

Topological defect engineering enables size and shape control in self-assembly

Lara Koehler,^{1,2,*} Markus Eder,^{3,*} Christoph Karfusehr,^{3,4} Vincent Ouazan-Reboul,¹ Pierre Ronceray,⁵ Friedrich C. Simmel,^{3,4} and Martin Lenz^{1,6,†}

¹Université Paris-Saclay, CNRS, LPTMS, 91405, Orsay, France

²Max Planck Institute for the Physics of Complex Systems, Dresden, Germany

³Department of Bioscience, School of Natural Sciences, Technical University of Munich, Garching, Germany

⁴Max Planck School Matter to Life, Jahnstraße 29, Heidelberg, D-69120, Germany

⁵Aix Marseille Université, CNRS, CINAM, Turing Center for Living Systems, 13288 Marseille, France

⁶PMMH, CNRS, ESPCI Paris, PSL University, Sorbonne Université, Université Paris-Cité, F-75005, Paris, France

(Dated: April 18, 2025)

The self-assembly of complex structures from engineered subunits is a major goal of nanotechnology, but controlling their size becomes increasingly difficult in larger assemblies. Existing strategies present significant challenges, among which are the use of multiple subunit types or the precise control of their shape and mechanics. Here we introduce an alternative approach based on identical subunits whose interactions promote crystals, but also favor crystalline defects. We theoretically show that topological restrictions on the scope of these defects in large assemblies imply that the assembly size is controlled by the magnitude of the defect-inducing interaction. Using DNA origami, we experimentally demonstrate both size and shape control in two-dimensional disk- and fiber-like assemblies. Our basic concept of defect engineering could be generalized well beyond these simple examples, and thus provide a broadly applicable scheme to control self-assembly.

Equilibrium self-assembly is a powerful way to build nano- and microscale structures out of well-designed subunits [1, 2]. Many biological and technological functions, however, require these structures to have a well-controlled size [3, 4], requiring specific strategies for self-limiting assembly [5]. In a first approach known as programmable assembly, a set of several distinct subunits bind with one another according to a predefined pattern of interactions [6–9]. The outer surface of a complete assembly is designed not to interact with any remaining subunits, leading to size limitation. A second strategy, self-closing assembly, uses identical subunits that bind at an angle. A collection of many such subunits forms a ring, a cylinder or a sphere whose closure terminates the assembly process [10–13]. A last pathway relies on deformable subunits whose shapes change upon binding to one another. In properly designed systems, these deformations increase as more and more subunits are added to the assembly, which eventually inhibits further growth [14–17].

Several experimental platforms enable these strategies, including DNA origami [18–20], and DNA tile assembly at the sub-micrometer scale [21, 22], as well as larger colloidal systems interacting through attached DNA strands [23–25] or through shape recognition mediated by depletion interactions [26–29]. However, the formation of large, self-limited assemblies remains challenging and requires pushing these techniques to their limits. Using large numbers of distinct subunits in programmable self-assembly can lead to high costs and low yields [30]. In self-closing assembly, both flexibility and small uncertainties in the subunit shapes lead to the formation of diverse, potentially off-target structures [13, 31]. Finally, deformable subunits are difficult to manufacture, and their elastic properties must be tightly controlled to avoid the formation of infinite assemblies.

Here we propose an alternative route to self-limiting assembly that circumvents these limitations. Our approach relies on a single type of lattice-forming subunits and does not require fine control over their shape or elasticity. Instead, the regulation of the assembly size and shape relies on the competition between two binding energies, which in DNA-based systems can be controlled to a high precision [32, 33]. As illustrated in Fig. 1a, the first energy is associated with subunits organizing into a crystalline lattice. The second describes defects in the crystal, specifically grain boundaries between domains with different orientations. Our strategy requires that unlike in usual (*e.g.*, metallic) crystals, the defect energy be

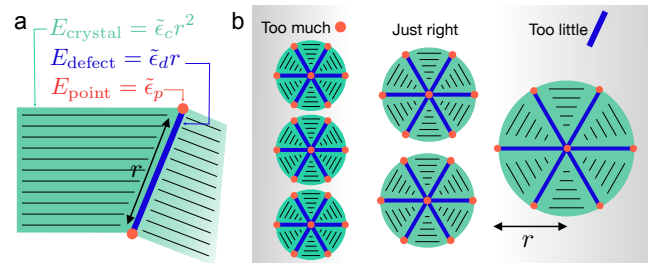


Figure 1. Crystals with energetically favorable defects may not grow to arbitrarily large sizes. **a.** Our proposed subunits form crystals with binding free energy $\tilde{\epsilon}_c < 0$, but also favor defective grain boundaries with $\tilde{\epsilon}_d < \tilde{\epsilon}_c$. Singular points at the end of these defects generically incur a cost $\tilde{\epsilon}_p > 0$ related to $\tilde{\epsilon}_d$ and $\tilde{\epsilon}_c$. Assuming the crystalline domains and defects are characterized by a single typical length r , the associated free energies respectively scale as $\tilde{\epsilon}_c r^2$, $\tilde{\epsilon}_d r^1$ and $\tilde{\epsilon}_p r^0$. **b.** Because these quantities scale differently with r , small assemblies are dominated by energetically costly singular points and large ones by crystalline interactions. The favorable defect interactions may dominate in assemblies with intermediate sizes, making them the most stable. Expressing r in units of the subunit size, this qualitative result is recovered by minimizing the free energy per subunit $\approx -|\tilde{\epsilon}_c| - |\tilde{\epsilon}_d|/r + |\tilde{\epsilon}_p|/r^2$, yielding a preferred radius $r \approx |\tilde{\epsilon}_p/\tilde{\epsilon}_d|$.

* These authors contributed equally to this work

† martin.lenz@universite-paris-saclay.fr

more favorable than that of the crystal. In this setting, subunits self-assemble into structures with a set number of defects imposed by topological constraints (see Supplementary Section S5). The crystalline interaction favors the formation of large assemblies, while forming a large number of small structures maximizes the defect interaction. As illustrated in Fig. 1b, the balance of these effects results in the emergence of an optimal assembly size set by the values of the interaction energies.

THEORY OF DEFECT-INDUCED SIZE LIMITATION

To formalize our proposal, we consider a set of identical hexagonal subunits that can bind to their neighbors through the short-range orientation-dependent interaction rules illustrated in Fig. 2a. The subunits bind through a crystalline or a defect interaction with binding energies ϵ_c and ϵ_d .

Tiling the plane using subunits with identical orientations gives rise to crystalline interactions everywhere. By contrast, there can be no dense tiling displaying defect interactions everywhere (proof in Supplementary Section S5). As a result, a large assembly that includes defect interactions must also comprise many additional crystalline interactions.

To determine the most favorable assembly structure, we express the energy of two idealized assembly geometries. We thus consider a piece of crystal in the shape of a regular hexagon (which maximizes the crystallization energy), and a six-fold symmetric assembly whose defects impose a vortex-like pattern of subunit orientations (inset of Fig. 2b). We reason that minimizing the total energy of a fixed number of subunits is equivalent to minimizing the average energy per subunit e , and express this quantity as a function of the assembly radius r for each structure (see Supplementary Section S3.1):

$$e_{\text{crystal}}(r) = \frac{9r^2 + 3r}{3r(r+1) + 1} \epsilon_c \quad (1a)$$

$$e_{\text{vortex}}(r) = \frac{3\epsilon_c r^2 + (-3\epsilon_c + 4\epsilon_d)r - 2\epsilon_d}{r(r+1)}. \quad (1b)$$

Here the crystalline case includes isolated monomeric subunits as its $r = 0$ case, while the $r = 1$ vortex assembly is the largest possible structure that includes only defect interactions, namely a ring-like hexamer. For large ($r \gg 1$) assemblies, Eq. (1b) recapitulates the discussion in the caption of Fig. 1 with $\tilde{\epsilon}_d = 4\epsilon_d - 6\epsilon_c$ and $\tilde{\epsilon}_p = 6(\epsilon_c - \epsilon_d)$.

We use Eqs. (1) to determine the most energetically favorable assembly as a function of the value of our interaction parameters, and display the result in Fig. 2b. This phase diagram reveals that the most favorable assembly depends only on the ratios of the two interaction parameters and their signs. Since the crystal energy Eq. (1a) is a monotonic function of r , crystalline ground states consist either in isolated monomers or in infinitely large crystals. By contrast, vortex assemblies display finite-size ground states that dominate the left-hand-side of the phase diagram. For attractive crystalline interactions ($\epsilon_c < 0$), the size of these assemblies diverges as the system approaches the $\epsilon_c = 2\epsilon_d/3$ line. This suggests that

any assembly size can be energetically favored under suitable conditions, which could enable size control over arbitrarily large assemblies.

To test the robustness of our conclusions against thermal fluctuations and assess the possible dominance of structures beyond our crystal and ideal vortex assembly, we numerically simulate the self-assembly process. We run a Monte Carlo simulated annealing down to a fixed finite temperature (see Supplementary Section S1.1 for details). We find an excellent qualitative agreement with our theory, whereby we recover all predicted structures in the right range of parameters (Fig. 2c). As shown in Fig. 2d, a straightforward finite-temperature extension of our theory accurately predicts the assembly size distribution.

DNA ORIGAMI IMPLEMENTATION

We implement our proposed six-fold subunit design using hollow DNA origami nanocylinders. Our subunits interact through a six-fold pattern of 16 nucleotide (nt) long single-stranded DNA origami linkers each comprising a 4 nt oligothymidine anchor domain at the 5' end for flexibility, followed by a 12 nt sticky domain designed to hybridize with its complementary sequence through base-pairing (Fig. 3a). The length and sequence of this sticky domain enable fine control of the hybridization free energy and ensure that it is associated with a melting temperature within the experimentally accessible range of $T = 25^\circ\text{C}$ - 40°C . The linkers are organized in three vertical layers along the height of the cylinder. The middle layer features one linker in each of the six binding directions and serves to implement a crystalline interaction ϵ_c ranging from -13 to $-9 \text{ kcal} \cdot \text{mol}^{-1}$ (approximately -21 to $-15 k_B T$ with $T = 36^\circ\text{C}$; see Fig. 3b and Supplementary Section S2.1). We implement each defect interaction using two pairs of linkers from the top and bottom layer. This allows us to probe the range $0.33 \leq \epsilon_c/\epsilon_d \leq 0.6$ relevant for self-limited assembly while retaining experimentally accessible melting temperatures.

We allow our nanocylinders self-assemble by incubating them at constant temperature $T = 36^\circ\text{C}$ for 20 hours in a buffer containing $[\text{MgCl}_2] = 5 \text{ mM}$, resulting in structures highly reminiscent of our theoretical predictions (Fig. 3c and Fig. S10). We further investigate the orientations of individual nanocylinders by labeling them at a single position with a 5 nm DNA-grafted gold nanoparticle, and find that they are consistent with our predicted vortex assemblies (Fig. 3d). We confirm this result by studying the distribution of orientations over a large number of assemblies. We find that adding Gaussian noise with a standard deviation of $\sigma_\varphi = 20^\circ$ to the ideal orientations, to account for effects such as the flexibility of the tether linking the gold nanoparticle to the nanocylinder, yields almost perfect agreement with the data (Fig. 3e, Kolmogorov-Smirnov test p-value $p = 0.65$). Taken together, these results demonstrate that our DNA nanocylinders indeed form the vortex assemblies underlying our size control mechanism.

We next quantitatively examine our size limitation mechanism by studying the distribution of assembly sizes (see Sup-

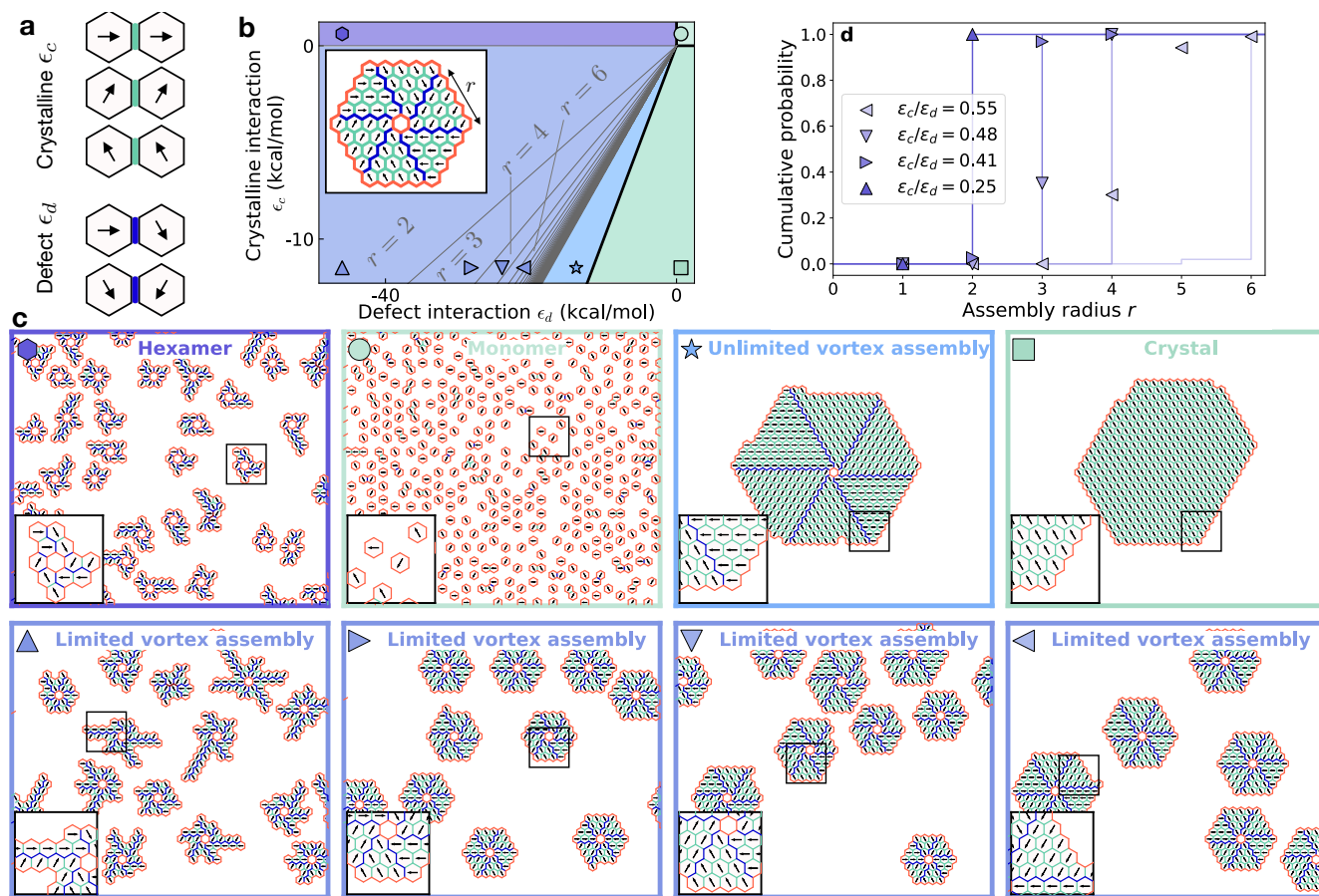


Figure 2. **Modeling demonstrates size control in randomly assembling subunits.** **a.** We consider hexagonal subunits with anisotropic two-body interactions materialized by colored patches. All relative binding orientations not pictured in this panel are strongly penalized in our model. **b.** Analytical phase diagram derived from Eqs. (1). *Colored symbols* point to the nomenclature defined in panel c. *Inset:* vortex assembly structure considered in our analytical calculations. **c.** Final structures of simulated assemblies for the parameter values marked by symbols in panel b. Long protrusions can form at the corner of the smallest assemblies, but are increasingly penalized for smaller values of ϵ_c/ϵ_d as discussed in the SI. **d.** Distributions of final assembly sizes at the end of the simulations and comparison with an ideal-gas-of-cluster theory applied to Eq. (1b) (see Supplementary Section S3.3). We observe some moderate deviations for the largest assembly sizes, hinting at the error committed by neglecting the entropy associated with fluctuations in the assembly shapes as well as by the effect of their nucleation kinetics.

plementary Section S1.2 and S2.3). In Fig. 3f we find that it does not markedly depend on the incubation time after 10 hours, suggesting that they are at equilibrium. We additionally vary the MgCl_2 concentration in our sample based on the fact that an increased salt concentration increases non-specific interactions in DNA origami (Fig. 3g). This does not lead to a significant change of our assembly sizes, indicating that the structures we observe are primarily based on specific hybridization interactions. Finally, Fig. 3h demonstrates that consistent with our theoretical predictions, the ratio of the crystalline to the defect hybridization energies controls the size of the assembly up to large radii, thus demonstrating our proposed size control mechanism.

SHAPE CONTROL THROUGH DEFECT ENGINEERING

Beyond the design and control of vortex assemblies, we suggest that defect engineering could be a general and ver-

satile self-assembly strategy. While its full potential remains to be explored, we here demonstrate additional possible design schemes and point out some of the challenges involved in developing more complex designs.

Our vortex design results from defect interactions that cause the subunit orientation to rotate clockwise when crossing a defect line (Fig. 2a). In Fig. 4a we instead consider defect interactions that reverse the arrow orientation. This new design again favors triangle-shaped crystalline domains, but as shown in the inset of Fig. 4b these form an alternating fiber-like pattern with an energy per subunit

$$e_{\text{fiber}}(r) = \frac{3\epsilon_c r^2 + (4\epsilon_d - 3\epsilon_c)r + 2(\epsilon_c - \epsilon_d)}{r(r+1)}. \quad (2)$$

As in the vortex case, this energy can display a minimum for a finite size r of the triangular domains. Fig. 4b shows the resulting phase diagram, which we further validate through numerical simulations (Fig. 4c). Finally, we implement this

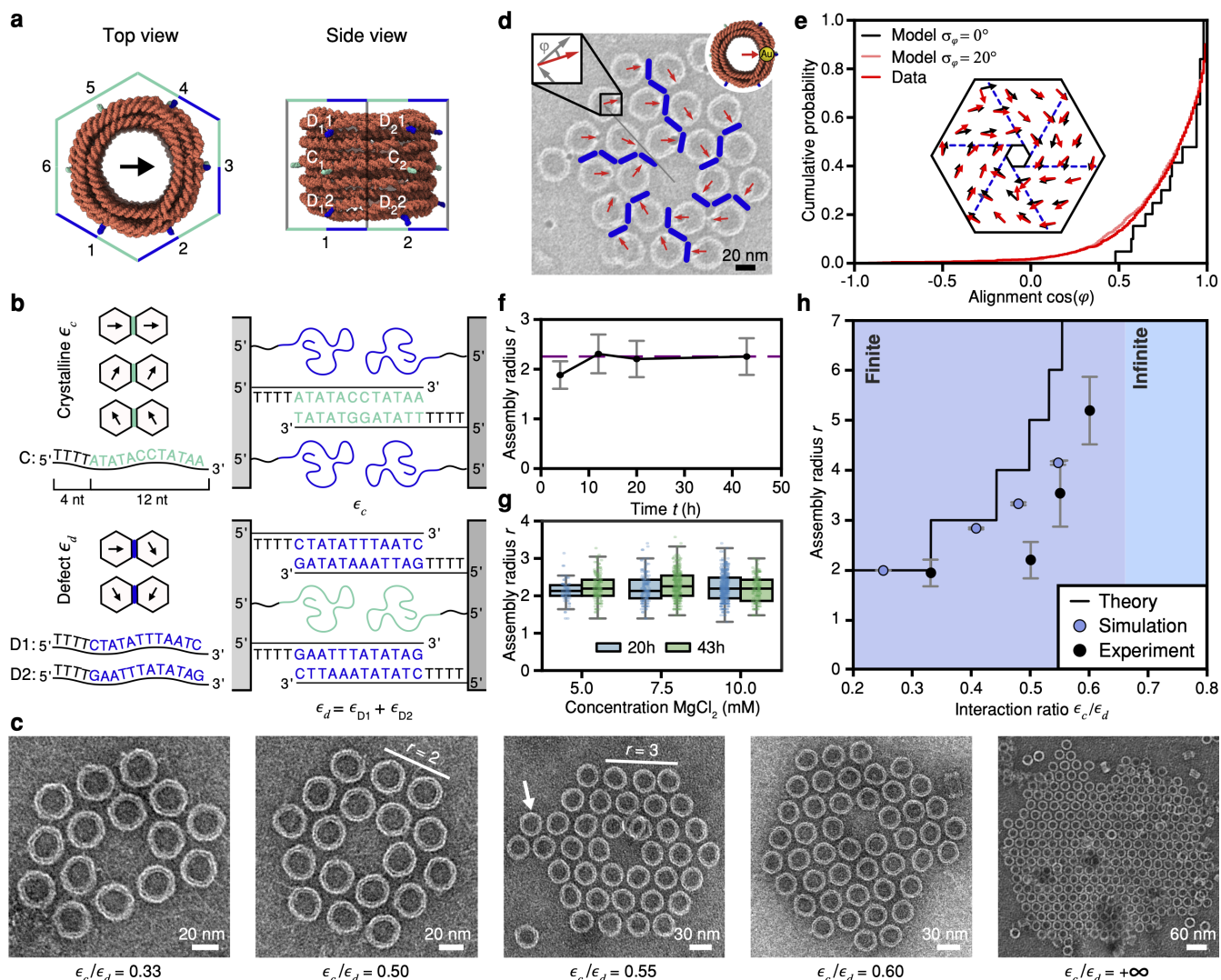


Figure 3. DNA origami nanocylinders form finite-size assemblies. **a.** Molecular model of our DNA origami subunits generated with OxDNA (see Supplementary Section S2.2). Light and dark blue linkers respectively provide the crystalline and defect interactions. **b.** Crystalline linkers on opposite sides of the subunit (e.g., sides 2 and 5) have complementary sequences, resulting in the hybridization pattern shown in the top row. The defect linkers remain unhybridized in this interaction. Conversely, a defect interaction (e.g., between sides 2 and 4) involves the hybridization of two pairs of defect linkers while the crystalline linkers remain unhybridized (bottom row). Sides 5 and 6 of the nanocylinders are never involved in defect interactions and do not carry any defect linkers. **c.** TEM micrographs of the assemblies formed by our nanocylinders illustrate the dependence of their radius on ϵ_c/ϵ_d . The corner protrusion highlighted by the white arrow resembles the defect-interaction-induced appendages observed in the numerical simulations of Fig. 2c (see Supplementary Figure S11 for more examples). **d.** Labeling of side 3 with gold nanoparticles (AuNP) reveals subunit orientations consistent with our vortex assembly design (red arrows), allowing us to point out likely defect interaction sites (dark blue segments). Here $\epsilon_c/\epsilon_d = 0.5$. **e.** The empirical distribution function of AuNP-labelled subunit orientations at $\epsilon_c/\epsilon_d = 0.5$ closely resembles an ideal $r = 3$ vortex assembly structure with noise added. Here we analyzed $N = 1375$ subunits from three independent experiments. **f.** The assembly size distribution is robust to variations in incubation time. Bars here and in the next panel represent Bessel corrected standard deviations. Here $[\text{MgCl}_2] = 5 \text{ mM}$. **g.** The assembly size distribution is robust to variations in salt concentration. Here we analyze $N_{20\text{h}} = 67$, $N_{43\text{h}} = 137$ assemblies at 5 mM, $N_{20\text{h}} = 131$, $N_{43\text{h}} = 278$ at 7.5 mM and $N_{20\text{h}} = 364$, $N_{43\text{h}} = 141$ at 10 mM. **h.** The assembly radius depends on the binding free energies as predicted by theory. Sample sizes are $N_{0.33} = 106$, $N_{0.5} = 562$, $N_{0.55} = 122$ and $N_{0.6} = 39$ for the experiments, and $N_{0.25} = 228$, $N_{0.41} = 223$, $N_{0.48} = 165$ and $N_{0.55} = 103$ for the simulations.

design using our six-fold DNA nanocylinder platform, and indeed observe the formation of fiber-like assemblies (Fig. 4d and Fig. S10).

Further repositionings of the defect interactions allow for multiple other size-controlled assemblies. The design of

Fig. 4e thus rearranges our triangular crystalline domains into a patterned bulk. We next explore two variants of the finite assemblies of Fig. 2. Rotating the subunit orientations by 120° instead of 60° upon crossing a defect abolishes the large-scale crystal domains and leads to star-like assemblies where all

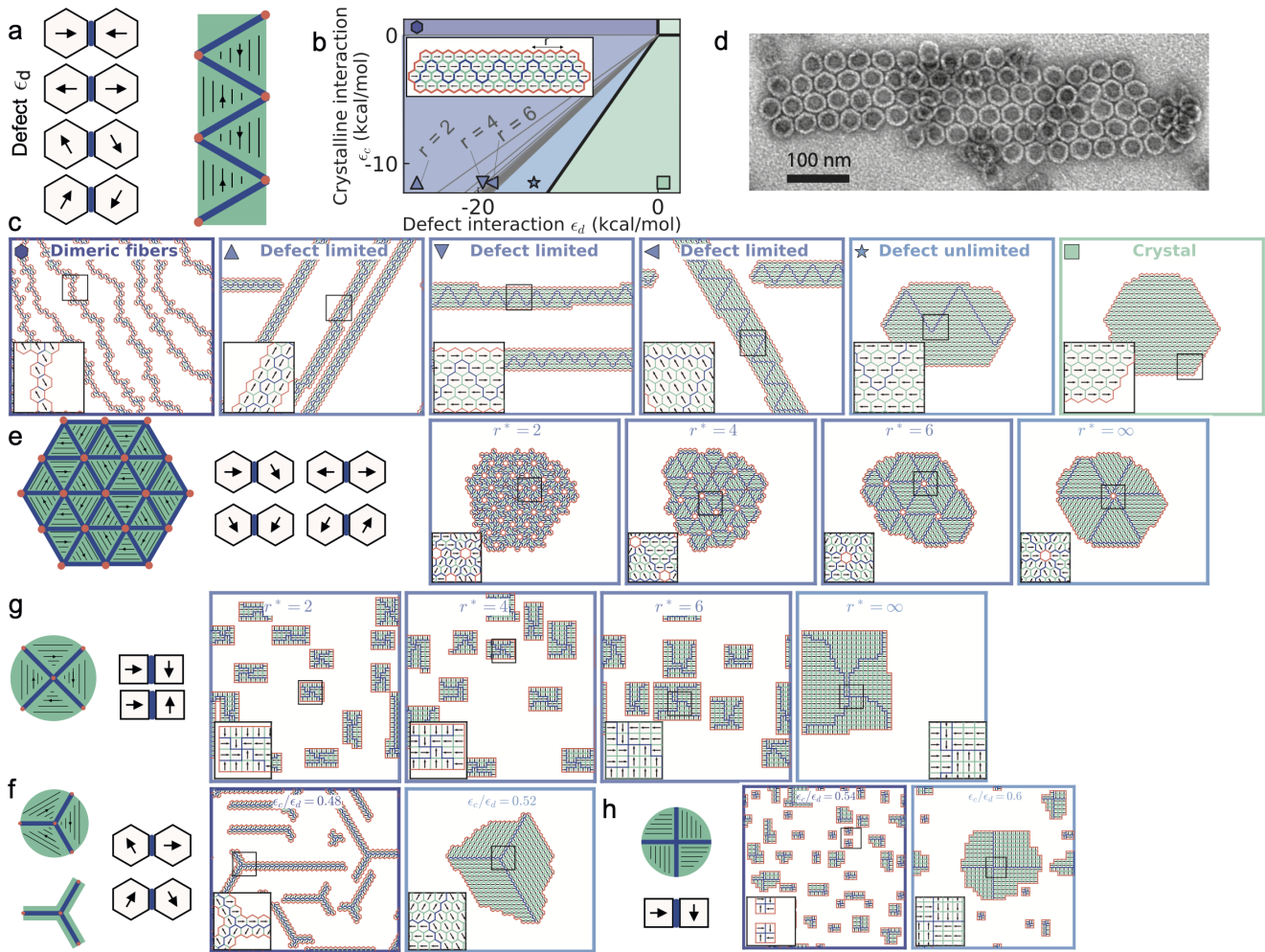


Figure 4. **Defect engineering provides a rich design space.** **a.** Defect interactions and conceptual schematic for fiber-like assemblies. Here and in the following crystalline interactions are present but not illustrated. **b.** Corresponding phase diagram derived from Eqs. (1a) and (2). This differs from the phase diagram of Fig. 2b only through differences in the slope of the diagonal lines. *Inset:* Detailed structure of an ideal fiber-like assembly. **c.** Simulations conducted using the same protocol as in Fig. 2c. **d.** TEM micrograph of a fibrous structure assembled at $\epsilon_c/\epsilon_d = 0.5$ with the same protocol as in Fig. 3. **e.** Patterned bulk design. **f.** Three-fold design leading to unlimited assemblies that transition from thin defect lines to bulk. **g.** Square size-limited design. **h.** An invalid design for two-dimensional self-limitation.

subunits are in contact with a defect line (Fig. 4f). By contrast, a design based on square subunits preserves finite-size assembly but features flexible defect lines (Fig. 4g). These lines form diagonal paths on a square lattice, implying that their length depends only on their total horizontal and vertical amplitude. This results in a high degeneracy, whereby any directed defect line that starts and ends at the corners of a square assembly yields the same overall energy. The entropy associated with this conformational freedom tends to favor large assemblies, and appears to make their overall shape more flexible in our simulations. In Fig. 4e we present an extension of our strategy to three dimensions based on a simple generalization of this square-lattice design. Finally, we point out the alternative design of Fig. 4h, which does not lead to size limitation, as a cautionary example of the subtleties of defect engineering: in this case the local symmetry of the interactions implies a vanishing $\bar{\epsilon}_p$ in the language of Fig. 1, and thus a function $e(r)$ that does not have a minimum

at finite r .

DISCUSSION

The induction of energetically costly grain boundaries has been used to design materials for centuries [34]. Here we propose to harness modern self-assembly techniques to instead make them energetically favorable. We find that this approach results in an energetic situation that resembles classical nucleation theory in reverse. In classical nucleation, an unfavorable boundary energy combined with a favorable bulk energy imply that clusters of intermediate sizes, the so-called critical nuclei, are unstable [35]. In our approach, the boundary energy stems not from the outer surface of the assembly, but from the grain boundaries within. Because it is favorable, it produces stable, finite clusters of arbitrarily large sizes and controllable morphologies in two and three dimensions.

Our strategy plays to the strengths of DNA nanotechnologies developed over the last two decades. In contrast with other self-limitation schemes [5], it can be implemented with a single subunit type and does not require fine control over their shape and elasticity. As in other designs however, controlling the morphology of large assemblies becomes increasingly difficult as their size r increases, and the minimum in the specific energy $e(r)$ becomes more and more shallow. Under such conditions the assembly nucleation kinetics can play a non-negligible role in determining the final assembly size, which could account for the modest discrepancies between our equilibrium theory and Monte Carlo simulations. This issue is less likely to influence our DNA origami implementation, which benefits from comparatively long equilibration times. Instead, the slight shift between the corresponding experimental data and our predictions may be due to our relatively crude estimate of the subunit binding free energy. This

estimate could be refined by taking into account other, *e.g.*, entropic, effects beyond base pairing.

A crucial requirement for our approach is the ability to favor only a few specific grain boundary interactions, resulting in topological restrictions that prevent their proliferation throughout the bulk. In our hexagonal subunit design, this is achieved by singling out two to four favorable interactions out of twenty-one [36] possible defect-inducing options. The implied number of unexplored choices hints at an enormous untapped design freedom. This freedom is further broadened when considering three-dimensional subunits, the possibility of assigning distinct energies to different defect interactions, or an independent control of the point energy $\tilde{\epsilon}_p$ through three-body or steric interactions between subunits. Exploring this enormous design space and understanding its structuring principles represents an exciting experimental and theoretical challenge, and could open new avenues in nanotechnology.

-
- [1] S. C. Glotzer and M. J. Solomon, Anisotropy of building blocks and their assembly into complex structures, *Nature materials* **6**, 557 (2007).
- [2] A. V. Pinheiro, D. Han, W. M. Shih, and H. Yan, Challenges and opportunities for structural DNA nanotechnology, *Nature nanotechnology* **6**, 763 (2011).
- [3] D. L. Caspar and A. Klug, Physical principles in the construction of regular viruses, in *Cold Spring Harbor symposia on quantitative biology*, Vol. 27 (Cold Spring Harbor Laboratory Press, 1962) pp. 1–24.
- [4] Y. Fu, D. Zeng, J. Chao, Y. Jin, Z. Zhang, H. Liu, D. Li, H. Ma, Q. Huang, K. V. Gothelf, *et al.*, Single-step rapid assembly of DNA origami nanostructures for addressable nanoscale bioreactors, *Journal of the American Chemical Society* **135**, 696 (2013).
- [5] M. F. Hagan and G. M. Grason, Equilibrium mechanisms of self-limiting assembly, *Reviews of modern physics* **93**, 025008 (2021).
- [6] K. Lund, Y. Liu, S. Lindsay, and H. Yan, Self-Assembling a Molecular Pegboard, *Journal of the American Chemical Society* **127**, 17606 (2005).
- [7] Y. Liu, Y. Ke, and H. Yan, Self-Assembly of Symmetric Finite-Size DNA Nanoarrays, *Journal of the American Chemical Society* **127**, 17140 (2005).
- [8] G. Tikhomirov, P. Petersen, and L. Qian, Fractal assembly of micrometre-scale DNA origami arrays with arbitrary patterns, *Nature* **552**, 67 (2017).
- [9] C. G. Evans and E. Winfree, Physical principles for DNA tile self-assembly, *Chemical Society Reviews* **46**, 3808 (2017).
- [10] K. F. Wagenbauer, C. Sigl, and H. Dietz, Gigadalton-scale shape-programmable DNA assemblies, *Nature* **552**, 78 (2017).
- [11] C. Sigl, E. M. Willner, W. Engelen, J. A. Kretzmann, K. Sachenbacher, A. Liedl, F. Kolbe, F. Wilsch, S. A. Aghvami, U. Protzer, M. F. Hagan, S. Fraden, and H. Dietz, Programmable icosahedral shell system for virus trapping, *Nature Materials* **20**, 1281 (2021).
- [12] T. E. Videbæk, D. Hayakawa, G. M. Grason, M. F. Hagan, S. Fraden, and W. B. Rogers, Economical routes to size-specific assembly of self-closing structures, *Science advances* **10**, eado5979 (2024).
- [13] D. Hayakawa, T. E. Videbæk, D. M. Hall, H. Fang, C. Sigl, E. Feigl, H. Dietz, S. Fraden, M. F. Hagan, G. M. Grason, *et al.*, Geometrically programmed self-limited assembly of tubules using DNA origami colloids, *Proceedings of the National Academy of Sciences* **119**, e2207902119 (2022).
- [14] M. Lenz and T. A. Witten, Geometrical frustration yields fibre formation in self-assembly, *Nature physics* **13**, 1100 (2017).
- [15] D. M. Hall, M. J. Stevens, and G. M. Grason, Building blocks of non-euclidean ribbons: size-controlled self-assembly via discrete frustrated particles, *Soft Matter* **19**, 858 (2023).
- [16] N. W. Hackney, C. Amey, and G. M. Grason, Dispersed, condensed and self-limiting states of geometrically frustrated assembly, *arXiv preprint arXiv:2303.02121* (2023).
- [17] J. F. Berengut, C. K. Wong, J. C. Berengut, J. P. Doye, T. E. Ouldridge, and L. K. Lee, Self-limiting polymerization of DNA origami subunits with strain accumulation, *ACS nano* **14**, 17428 (2020).
- [18] P. W. Rothmund, Folding DNA to create nanoscale shapes and patterns, *Nature* **440**, 297 (2006).
- [19] S. M. Douglas, H. Dietz, T. Liedl, B. Högberg, F. Graf, and W. M. Shih, Self-assembly of DNA into nanoscale three-dimensional shapes, *Nature* **459**, 414 (2009).
- [20] S. Dey, C. Fan, and K. V. e. a. Gothelf, DNA origami, *Nature Reviews Methods Primers* **1**, 10.1038/s43586-020-00009-8 (2021).
- [21] B. Wei, M. Dai, and P. Yin, Complex shapes self-assembled from single-stranded DNA tiles, *Nature* **485**, 623 (2012).
- [22] Y. Ke, L. L. Ong, W. M. Shih, and P. Yin, Three-dimensional structures self-assembled from DNA bricks, *Science* **338**, 1177 (2012).
- [23] S. Y. Park, A. K. R. Lytton-Jean, B. Lee, S. Weigand, G. C. Schatz, and C. A. Mirkin, DNA-programmable nanoparticle crystallization, *Nature* **451**, 553 (2008).
- [24] D. Nykpanchuk, M. M. Maye, D. v. d. Lelie, and O. Gang, DNA-guided crystallization of colloidal nanoparticles, **451**, 549 (2008).
- [25] C. A. Mirkin and S. H. Petrosko, Inspired Beyond Nature: Three Decades of Spherical Nucleic Acids and Colloidal Crystal Engineering with DNA, *ACS Nano* **17**, 16291 (2023).
- [26] P. L. Biancaniello, A. J. Kim, and J. C. Crocker, Colloidal interactions and self-assembly using DNA hybridization, *Phys. Rev. Lett.* **94**, 058302 (2005).
- [27] A. McMullen, M. Muñoz Basagoiti, Z. Zeravcic, and J. Brujic, Self-assembly of emulsion droplets through programmable

- folding, *Nature* **610**, 502 (2022).
- [28] S. Sacanna, W. T. Irvine, P. M. Chaikin, and D. J. Pine, Lock and key colloids, *Nature* **464**, 575 (2010).
- [29] T. Tigges and A. Walther, Hierarchical self-assembly of 3d-printed lock-and-key colloids through shape recognition, *Angew. Chem. Int. Ed.* **55**, 11261 (2016).
- [30] M. H. Huntley, A. Murugan, and M. P. Brenner, Information capacity of specific interactions, *Proceedings of the National Academy of Sciences* **113**, 5841 (2016).
- [31] A. Fotin, Y. Cheng, P. Sliz, N. Grigorieff, S. C. Harrison, T. Kirchhausen, and T. Walz, Molecular model for a complete clathrin lattice from electron cryomicroscopy, *Nature* **432**, 573 (2004).
- [32] J. SantaLucia, A unified view of polymer, dumbbell, and oligonucleotide DNA nearest-neighbor thermodynamics, *Proceedings Of The National Academy Of Sciences Of The United States Of America* **95**, 1460 (1998).
- [33] J. N. Zadeh, C. D. Steenberg, J. S. Bois, B. R. Wolfe, M. B. Pierce, A. R. Khan, R. M. Dirks, and N. A. Pierce, NUPACK: Analysis and design of nucleic acid systems, *J. Comput. Chem.* **32**, 170 (2011).
- [34] A. Williams, *The Sword and the Crucible: A History of the Metallurgy of European Swords up to the 16th Century*, *History of Warfare*, Vol. 77 (Brill, 2012).
- [35] D. W. Oxtoby, Homogeneous nucleation: theory and experiment, *Journal of Physics: Condensed Matter* **4**, 7627 (1992).
- [36] L. Koehler, P. Ronceray, and M. Lenz, How do particles with complex interactions self-assemble?, *Phys. Rev. X* **14**, 041061 (2024).

Topological defect engineering enables size and shape control in self-assembly

Supplementary Information

Lara Koehler,^{1,2,*} Markus Eder,^{3,*} Christoph Karfusehr,^{3,4} Vincent Ouazan-Reboul,¹ Pierre Ronceray,⁵ Friedrich C. Simmel,^{3,4} and Martin Lenz^{1,6,†}

¹*Université Paris-Saclay, CNRS, LPTMS, 91405, Orsay, France*

²*Max Planck Institute for the Physics of Complex Systems, Dresden, Germany*

³*Department of Bioscience, School of Natural Sciences,*

Technical University of Munich, Garching, Germany

⁴*Max Planck School Matter to Life, Jahnstraße 29, Heidelberg, D-69120, Germany*

⁵*Aix Marseille Université, CNRS, CINAM, Turing Center for Living Systems, 13288 Marseille, France*

⁶*PMMH, CNRS, ESPCI Paris, PSL University,*

Sorbonne Université, Université Paris-Cité, F-75005, Paris, France

(Dated: April 18, 2025)

Contents

S1. Numerical Materials and Methods	2
1. Simulation and Annealing Protocol	2
2. Measurement of Assembly Radius with Simulation	2
S2. Experimental Materials and Methods	4
1. Design of Interactions and Subunit Simulation	4
2. Experimental Protocols	5
3. Data Acquisition and Analysis	6
S3. Theory of Defect-Induced Size Limitation	8
1. Phase Diagram of the Vortex Assembly	8
2. Generalization of the Defect Engineering Principle	11
3. Entropic Effect Influences the Equilibrium Size Distribution	14
S4. Enhanced Theory–Simulation Agreement via Extended Annealing	17
S5. Geometrical Considerations	17
1. Interpolation of a Field Theory	19
2. Continuum Expression for the Defect Energy	19
3. Upper Bound on the Number of Defect Interactions	19
4. Topological and Energetic Constraints Resulting from the Interaction Rules	21
S6. Supplementary Figures	24
S7. Supplementary Tables	29
References	36

* These authors contributed equally to this work

† martin.lenz@universite-paris-saclay.fr

S1 Numerical Materials and Methods

To verify the theoretical prediction of self-limitation in the main text, we simulate annealing on a lattice for hexagonal and square subunits, following the interaction rules described in Fig. 2a of the main text. We use these simulations to generate the snapshots and associated assembly size distributions in Fig. 2 and Fig. 4 of the main text. Here, we first describe the simulation protocols and parameter choices in detail in Section S1.1, and then explain how we measure assembly sizes in the simulation in Section S1.2.

1 Simulation and Annealing Protocol

We perform simulated annealing with lattice subunits interacting as described in Fig. 2a of the main text. Here, we discuss the annealing protocol and report the parameters for all simulations presented in the main text.

We use a two-dimensional triangular lattice of 40×40 sites populated with 400 subunits. We perform simulated annealing by linearly increasing the inverse temperature $1/k_B T$ from 0 to 1 in 2000 increments. For each temperature increment, we perform $A = 4 \times 10^6$ Monte Carlo steps (which corresponds to 10^4 steps per subunit). One Monte Carlo move is attempted at each step and may involve either a single subunit, or several of them. Single-subunit moves consist in either a rotation of a single subunit, or the transfer of a subunit to an unoccupied site, which we refer to as a translation. Collective moves involve a hexagonal plaquette comprised of multiple sites, among which at least one is occupied, and may consist in either a rotation of the plaquette, or of a translation to a plaquette of empty lattice sites of identical size. Each Monte Carlo move is accepted according to the Metropolis criterion. We denote by α the rate of collective Monte Carlo moves, and attempt single-subunit rotations and single-subunit translations each with probability $(1 - \alpha)/2$, and plaquette rotation and plaquette translation each with probability $\alpha/2$.

The energies involved in our simulations are most naturally expressed in units of $k_B T$, while the binding free energies in the experiments are typically listed in kcal/mol. Assuming a temperature of $36^\circ C = 309.15 K$ as during the assembly stage in our experiments, the correspondence is $1 \text{ kcal/mol} = 1.628 k_B T/\text{subunit}$.

Therefore, a binding energy of -11.54 kcal/mol , which is the typical binding energy used in the experiments, corresponds to an interaction energy between two subunits of $-18.7 k_B T$. For all the simulations in the size-limitation region, we choose $\epsilon_c = -18.7 k_B T/\text{subunits} = -11.54 \text{ kcal/mol}$.

We summarize the parameter values for all our simulations in Table S1.

2 Measurement of Assembly Radius with Simulation

We now show how we use the simulation results to measure the assembly size distribution. For each assembly within an annealed system, we automatically count its number of subunits N and its number of interfaces between a subunit and an empty site S , as illustrated in Fig. S1. As shown in Fig 2c. of the main text, some vortex assemblies have extended grain-boundaries, which we here refer to as branches. To measure the assembly radius r , we assume that all assemblies have the geometry illustrated in Fig. S1. We use Eq. (1) to determine r and b , the number of subunits within the branches, from N and S for each assembly in the simulation as

$$N = 3r(r + 1) + b \quad (1a)$$

$$S = 6(2r + 1) + 2b. \quad (1b)$$

To obtain sufficient statistics on the assembly shapes, we repeat our simulated annealing 20 times. This yields a total of respectively 228, 223, 165 and 103 vortex assemblies, for the ratios ϵ_c/ϵ_d listed in Fig. 2d of the main text. We then directly determine the number of assemblies of radius r , $m(r)$, within all those simulations, regardless of the length of their branches b . The averaged radius in the simulations shown in Fig. 3h of the main text is $\sum_k km(k)/\sum_k m(k)$. The measured cumulative probabilities $P_r(k \leq r)$ shown in Fig. 2d of the main text are given in Eq. (2). r is an integer in the idealized geometry of Fig. S1, but we sum over all values extracted from the simulations, integer or not.

$$P_r(k \leq r) = \frac{\sum_{k \leq r} m(k)}{\sum_k m(k)} \quad (2)$$

These measurements allow us to directly assess the impact of the binding energy ratio (ϵ_c/ϵ_d) on the assembly size. They also enable us to compare the simulation results directly with the theoretical predictions and with the experiments.

Assembly type	Fraction of collective moves α	Number of annealing steps A	Crystalline interaction ϵ_c	Defect interaction ϵ_d	ϵ_c/ϵ_d	Forbidden interaction ϵ_f
6-fold vortex	0	5×10^8	-18.7	-74.8	0.25	10
6-fold vortex	0	5×10^8	-18.7	-45.9	0.407	10
6-fold vortex	0	5×10^8	-18.7	-39.0261	0.479	10
6-fold vortex	0	5×10^8	-18.7	-34.2305	0.546	10
6-fold vortex	5×10^{-2}	4×10^6	-18.7	-22.44	5/6	10
6-fold vortex	5×10^{-2}	4×10^6	1	-74.8		10
6-fold vortex	5×10^{-2}	4×10^6	-18.7	1		10
6-fold vortex	5×10^{-2}	4×10^6	1	1		10
Fiber	5×10^{-2}	4×10^6	-18.7	-43.6333	0.43	50
Fiber	5×10^{-2}	4×10^6	-18.7	-31.7087	0.59	50
Fiber	5×10^{-2}	4×10^6	-18.7	-30.1102	0.62	50
Fiber	5×10^{-2}	4×10^6	-18.7	-22.44	5/6	50
Fiber	5×10^{-2}	4×10^6	-18.7	1		50
Fiber	5×10^{-2}	4×10^6	1	-43.6		50
3-fold vortex	5×10^{-2}	4×10^6	-18.7	-38.9583	0.48	50
3-fold vortex	5×10^{-2}	4×10^6	-18.7	-35.9615	0.52	50
4-fold vortex	0	4×10^6	-18.7	-31.1667	0.6	10
4-fold vortex	0	4×10^6	-18.7	-29.3857	0.64	10
4-fold vortex	0	4×10^6	-18.7	-28.9	0.65	10
4-fold vortex	0	4×10^6	-18.7	-22.44	5/6	10
Invalid design	0	4×10^6	-18.7	-34.63	0.54	10
Invalid design	0	4×10^6	-18.7	-31.16	0.6	10
Patterned bulk	5×10^{-2}	4×10^6	-18.7	-49.8667	0.375	10
Patterned bulk	5×10^{-2}	4×10^6	-18.7	-26.0174	0.719	10
Patterned bulk	5×10^{-2}	4×10^6	-18.7	-22.8203	0.819	10
Patterned bulk	5×10^{-2}	4×10^6	-18.7	-18.7	1	10

Table S1. **Parameters.** The interaction energies ϵ_c, ϵ_d and ϵ_f are expressed in units of $k_B T$. In our simulations we associate a large positive “forbidden interaction” ϵ_f to all interfaces that are neither of the crystalline nor of the defect type to prevent them from occurring.

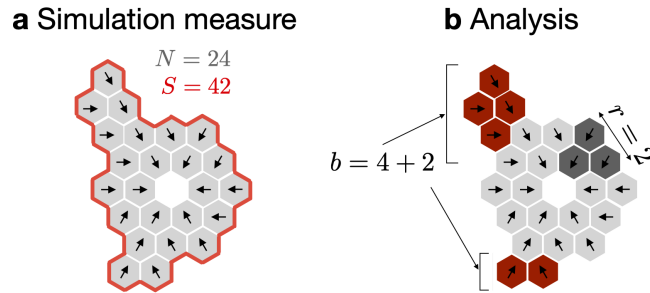


Figure S1. **We measure the assembly size N and surface S in the simulation and deduce the vortex assembly radius r and branch size b .** (a) N is the number of subunits in the assembly and S is the number of subunit edges in contact with an empty site outside of the assembly. (b) The vortex radius r is the size of a triangular crystalline domain (in dark gray) and the total branch length b is the number of subunits within a branch (in dark red).

S2 Experimental Materials and Methods

To experimentally verify our theoretical predictions and numerical findings, we implement a self-limiting assembly process using DNA origami nanocylinders that interact via base-pairing under predefined interaction rules. In Section S2.1, we describe the design of the DNA interaction strands that implement these rules, as well as the oxDNA simulation used to visualize the structure of the DNA origami subunit. In Section S2.2, we then detail the protocols for DNA origami folding, assembly, and functionalization with gold nanoparticles, which yield the experimental data for Fig. 3 of the main text. Finally, in Section S2.3, we outline the procedures for data acquisition and analysis.

1 Design of Interactions and Subunit Simulation

In this subsection, we first explain how the DNA interaction strand sequences for defect and crystalline interactions, as shown in Fig. 3b and listed in Table S5, were designed and selected to ensure the precise interaction energies (and their ratios) required for self-limiting assembly. We then describe how the oxDNA simulation framework, integrated within oxView, was used to generate the visual representation of the DNA origami nanocylinder’s mean structure shown in Fig. 3a.

Interaction Strand Design with NUPACK

Orthogonal defect and crystalline DNA interaction strand sets with specified Gibbs free energy differences (ϵ_d and ϵ_c) were designed using the NUPACK Python package [1]. Initially, exhaustive libraries of all possible sequences of lengths 10, 11, and 12 nucleotides, along with their reverse complements, were generated. For each sequence, relevant properties such as the Gibbs free energy (ϵ) of the minimum free energy (MFE) proxy structure and the secondary structure were calculated (model: dna04, temperature: 36 °C, sodium: 50 mM, magnesium: 5 mM, concentration: 10 nM). The sequence library of appropriate length was then filtered for sequences that exhibit no secondary structure with Gibbs free energy changes upon binding within a narrow tolerance interval $[\epsilon_d - \delta\epsilon_d, \epsilon_d + \delta\epsilon_d]$, centered around the intended value ϵ_d of the defect interaction. An initial tolerance of $\delta\epsilon_d = 0.05 \text{ kcal mol}^{-1}$ was applied. If this resulted in too few sequences, $\delta\epsilon_d$ was incrementally increased by $0.1 \text{ kcal mol}^{-1}$ until a sufficient number of candidates (typically a few hundred) was obtained. The same filtering criteria were subsequently applied to the original sequence library using ϵ_c to identify potential crystalline interaction strands. This process yielded sets of defect and crystalline interactions comprising n_d and n_c sequences, respectively.

To ensure intraset orthogonality, these sets were evaluated based on the bound fraction — defined as the ratio of DNA strands that are correctly bound to their intended reverse complementary partners to the total number of strands — if all strands in a set were mixed at a concentration of 10 nM each, with the maximum allowed assembly size set to two. Specifically, sets were deemed orthogonal if at least 90% of the defect interaction strands and at least 10% of the crystalline interaction strands bound exclusively to their intended partners. Sets failing to reach these orthogonality thresholds were excluded from further analysis. After identifying orthogonal defect and crystalline sets, all possible pairings of one defect set with one crystalline set were generated to form combined sets comprising $n_d + n_c$ sequences. These new combined sets then underwent an additional intraset orthogonality check to prevent unintended interactions. Specifically, any set exhibiting binding domains of six or more consecutive base pairs between strands that are not intended to form complementary pairs was disregarded as potential candidate for a valid interaction strand set.

From the remaining fully processed interaction strand sets, candidates were randomly selected and manually inspected for potential issues, such as the formation of G-quadruplex structures and long single-base repetitions. Finally, these selected sets were validated using the NUPACK web interface [2]. The sequence sets used in the experiments are listed in Table S5.

OxDNA Simulation

The DNA origami topology and configuration files for the nanocylinder were exported from a scadnano [3] design file (see Fig. S13), imported into oxView [4] and manually pre-arranged, for structure relaxation. Forces used during relaxation were automatically generated in oxView, and a Molecular Dynamics (MD) relaxation step was run on GPUs (ox-serve with nanobase.org webserver; first Bussi-Donadio-Parrinello then Brownian thermostat). Next, a

MD simulation was employed (oxDNA2 model [5], 1e9 steps) to simulate the monomer structure. The PDB file for rendering in ChimeraX was generated with the oxDNA analysis tools command line script [6]. The monomer structure shown in Fig. 3a of the main text represents a mean structure.

2 Experimental Protocols

This subsection outlines the experimental protocols employed throughout this work. First, we describe how the DNA origami nanocylinder is folded using an annealing ramp, followed by the purification steps to remove incomplete or misfolded structures. We then detail the procedure for assembling properly folded nanocylinders at different experimental conditions (Fig. 3f). Finally, we explain how gold nanoparticles are functionalized and attached to infer the assemblies' topological structure as exemplified in Fig. 3d.

DNA Origami Folding

The DNA origami nanotubes used in this study were originally developed by Wickham et al. [7]. Single-stranded p2873 DNA (scaffold strand, for sequence information see Table S3) was provided by Prof. Hendrik Dietz' group (100 nM in ddH₂O). Staple strands were purchased unpurified from Integrated DNA Technologies in 1× TE buffer (10 mM TRIS, 0.1 mM EDTA, pH 8.0) at 200 μM each (for sequence information see Table S4 and Table S5). Folding reactions were prepared with 50 nM scaffold strand and 200 nM staple strands in 1× FoB18 buffer (5 mM TRIS, 1 mM EDTA, 5 mM NaCl, 18 mM MgCl₂). Folding reactions were annealed in a thermocycler (Eppendorf, Mastercycler nexus GX2). The used protocol was 5 min incubation at 65 °C followed by an annealing ramp of −0.1 °C per 36 s from 60 °C to 30 °C. Folded DNA origami samples were immediately collected for purification.

DNA Origami Purification

Samples were purified using an ultrafiltration protocol. A centrifuge (Eppendorf, Centrifuge 5425 R) was pre-heated to 32 °C containing one 2 mL eppi 1× FoB5 washing buffer (5 mM TRIS, 1 mM EDTA, 5 mM NaCl, 5 mM MgCl₂) per sample. Amicon filters (Amicon Ultra 0.5 ml Ultracel 100k) were placed into 2 mL eppis, loaded with 500 μL pre-heated 1× FoB5 washing buffer and centrifuged (5 min, 10 krcf). The supernatant was discarded. Filters were loaded with 60 μL sample solution and 440 μL washing buffer and centrifuged (5 min, 10 krcf). The supernatant was discarded. Filters were then loaded with 500 μL washing buffer and centrifuged (5 min, 10 krcf). The supernatant was discarded once more. Filters were then loaded with 500 μL of 1× FoBX assembly buffer (5 mM TRIS, 1 mM EDTA, 5 mM NaCl, X =[5 mM, 7.5 mM, 10 mM] MgCl₂) with X being the MgCl₂ concentration used in the experiments as indicated in the main text. The filters were centrifuged (5 min, 10 krcf) one last time. Purified and buffer-adjusted samples were extracted from filters with a pipette by repeatedly aspirating and dispensing the solution to dissolve any potential pellets.

DNA Origami Assembly

The sample concentration was measured at 260 nm (Implen, NanoPhotometer N50) and normalized to 20 nM with assembly buffer (1× FoB5, 1× FoB7.5 or 1× FoB10). Samples were incubated in a thermocycler at 36 °C for varying amounts of time as indicated in the main text and resulting assemblies are immediately applied to TEM grids.

Functionalization of Gold Nanoparticles

To fabricate the DNA-grafted gold nanoparticles (DNA-AuNPs) with a freeze-thaw protocol [8], 110 μL of 90.8 nM AuNPs (Cytodiagnosics, d=5 nm) in 0.01× PBS buffer (0.1 mM) were mixed with 30 μL of HPLC purified 5'-thiol modified 20 nt poly-thymidine DNA strands (Biomers, lyophilized, resuspended to 100 μM in ddH₂O) and 860 μL of ddH₂O to an AuNP:DNA ratio of 1:300. The suspension was stored at −80 °C for 1 h and subsequently thawed at room temperature. Functionalized particles were purified by ultrafiltration with an Amicon filter (Amicon Ultra 0.5 ml Ultracel 100k). The filter was pre-washed with 500 μL of ddH₂O, centrifuged (14 krcf, 5 min) and the supernatant was discarded. Next, 500 μL of DNA-AuNP sample was loaded, centrifuged (14 krcf, 5 min) and

supernatant discarded. This step was repeated once. The sample was washed seven times by loading 500 μL of ddH₂O, centrifugating (14 krcf, 5 min) and discarding the supernatant. Finally, the filter was placed into a new eppi in inverse orientation and centrifuged (14 krcf, 5 min) to retrieve purified DNA-AuNPs in ddH₂O. The concentration of the AuNPs was then measured at 520 nm (Implen, NanoPhotometer N50) and the result of that measurement formed the basis of our dilution of the AuNPs to the standardized concentration used in our labeling experiments.

3 Data Acquisition and Analysis

First, we detail how the data were acquired using a transmission electron microscope to capture images of the assemblies. Next, we explain how vortex assembly sizes were determined from these TEM micrographs using the *scikit-image* Python library, thus enabling the generation of assembly size distributions and the calculation of mean assembly radii (Fig. 3h). Finally, we describe the evaluation method used to determine subunit orientation statistics for Fig. 3e.

Acquisition of TEM Micrographs

For TEM imaging, 5 μL of sample solution were incubated on glow-discharged (Electron Microscopy Sciences, K100X; 20 s, 35 mA, negative polarity) formvar carbon Cu400 TEM grids (Science Services) for 5–20 min. The staining solution was prepared by adding 1 μL of 5 M NaOH to 200 μL of a 2% uranyl formate solution, 10 s vortexing and subsequent centrifugation (2.5 min, 21 krcf). After sample incubation, grids were washed with 5 μL of staining solution and incubated with 20 μL of stain for 25 s. Automated imaging series were conducted with a FEI Tecnai T12 (120 kV) equipped with a Tietz TEMCAM-F416 camera, operated with SerialEM. Further sample imaging was conducted with a Philips CM100 (100 kV) operated with AmtV600.

Determination of Assembly Sizes

TEM image stacks were automatically pre-processed by monomer template matching, assembly recognition and calculation of properties with a custom Python script using the *scikit-image* library [9]. The cropped image of a DNA origami monomer was used as a template to match and extract all monomer instances from the first two TEM images in a stack. The average of all instances was calculated and the result used as an optimized template (now adjusted to the imaging conditions of the stack). For every image in a stack, areas occupied by monomers were matched with the optimized template and used as a mask to convert the image to a binary format. Pixels contained in the mask were set to 1, otherwise they were set to 0 (see Fig. S2a). Small gaps between features (pixels set to 1) were closed by using the *skimage.morphology.closing()* method, creating connected areas representing assemblies (see Fig. S2b). Resulting assemblies were labeled with unique identifiers by classifying pixels to be in the same assembly if they neighbor one another and have the same value (see Fig. S2c).

As shown in Fig. S2c, many of the objects in our electron microscopy images are isolated subunits or small clusters thereof. Each of these objects is assigned a label under the assembly-detection scheme described above. To set them aside from properly assembled vortex assemblies, different assembly properties (bounding box, area, perimeter, and centroid) were extracted for each labelled assembly with the *scikit.image.regionprops()* method. Assemblies were checked for the characteristic central hole, present in vortex assemblies. If hole size, hole eccentricity and monomer neighbor count were correct (a hole must have exactly six neighboring monomers), assemblies were marked as potential candidates and the number of monomers they contained was determined (Fig. S2d). Marked assemblies were individually presented with their extracted properties and their monomer count N manually validated. To obtain a continuous value for the intrinsically discrete assembly size r from N , an ideal vortex assembly was assumed and Eq. (1)a was solved with $b = 0$ to find

$$r = \frac{1}{2} \left(\sqrt{1 + \frac{4N}{3}} - 1 \right), \quad (3)$$

which was used in Figs. 3f-h of the main text. Images of vortex assemblies that were identified using this protocol were saved with their corresponding assembly properties and size r , then used in the analysis presented in the main text.

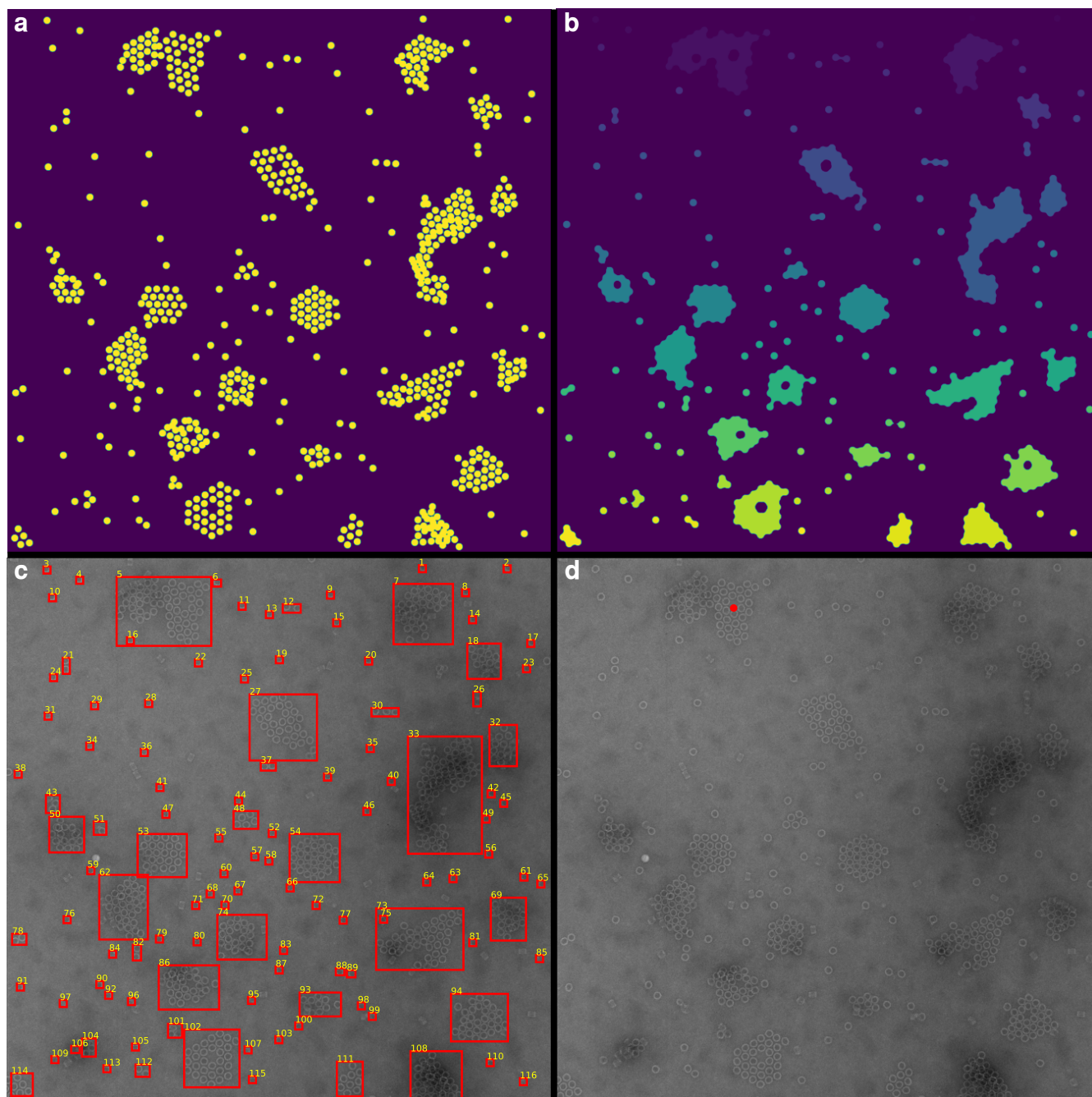


Figure S2. **Automated processing of TEM micrographs with a custom Python script using the *scikit-image* library.** **a.** Individual DNA origami nanocylinders are detected by template matching. **b.** Closed areas representing assemblies are created by using the `skimage.morphology.closing()` method. **c.** Assemblies are labeled with unique identifiers by using the `skimage.measure.label()` method with the 2-connectivity criterion. **d.** Filtering for valid vortex assembly candidates is done by checking for the existence and correct size and eccentricity of the characteristic central hole and the presence of exactly six monomers encircling the hole. If all criteria are met, the assembly is saved as candidate for manual validation. The red dot marks the central hole of one such candidate.

Determination of Subunit Orientations

To evaluate the orientations of subunits labeled with gold nanoparticles (AuNP), assemblies were extracted from TEM image stacks as described above. Using a custom Python script, assembly images were individually presented for manual processing. Images were mirrored horizontally if the majority of monomers in an assembly exhibited a counter-clockwise direction of rotation. For every AuNP labeled monomer in an assembly, a vector \mathbf{x}_i was drawn

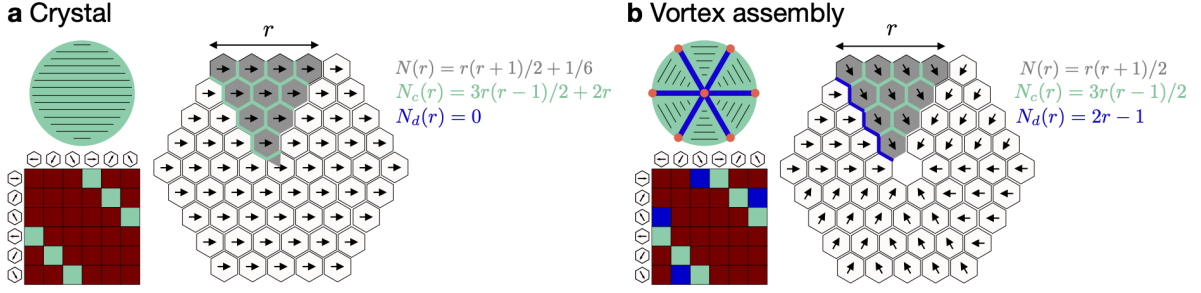


Figure S3. **Assembly geometries depend on the favored interactions.** For both (a) crystal and (b) vortex assemblies, we show the assembly schematic. We also show all possible contacts in an interaction map, where the crystalline interaction is colored in green, the defect interaction in blue, and all the other in dark red. For each pair, the orientation of the left and right subunits is read in the boundary and column entries. We compute the energy of the assembly by counting each the occurrence of crystal and defect interactions in a region of the assembly, as well as its total number of subunits.

from the monomer center to the AuNP position. A second vector \mathbf{y}_i was drawn center-to-center between the central hole in the assembly and the monomer. After processing all images, vectors \mathbf{x}_i and \mathbf{y}_i were normalized and their 2D cross product $\hat{\mathbf{x}}_i \times \hat{\mathbf{y}}_i = \cos \phi$ was computed. The results are displayed in Fig. 3e of the main text.

S3 Theory of Defect-Induced Size Limitation

In this section, we show how the binding energies influence the shape and the size of our vortex assemblies, leading to the phase diagram of Fig. 2 of the main text, as well as the numerical and theoretical assembly size distributions. We also show how repositioning the defect interactions yields diverse size-controlled assemblies, shown in Fig. 4 of the main text. In Section S3.1, we build the phase diagram of an idealized vortex assembly, including the thermodynamic prediction for the assembly radius. In Section S3.2 we present the energy per subunit of alternative assembly geometries with different numbers of defect lines, or topologies, presented in Fig. 4 of the main text. Finally, in Section S3.3, we show how to account for the finite temperature effects in the size prediction of the assemblies. These predictions are used in Fig. 2d of the main text.

1 Phase Diagram of the Vortex Assembly

We calculate the energy per subunit for a vortex assembly and for a crystal, as a function of their radius r . From these expressions, we determine the radius minimizing both energies, as well as which of the two assembly geometries is most stable, given the interaction energies ϵ_c and ϵ_d . This leads to the phase diagram in Fig. 2b of the main text.

Energy Calculation

Here, we determine the energy per subunit for the crystal and the vortex assembly. The energy of the total assembly is determined by its number of crystal interactions and defect interactions. We assume that the total number of subunits in the assembly is such that the radius r is an integer and the assembly is a perfectly symmetric hexagon. Therefore, we can simplify the calculations and compute the energy of a crystalline triangular tile, corresponding to $1/6^{\text{th}}$ of the assemblies.

Then, $1/6$ of an assembly has a number of defects $N_d/6$ and a number of crystalline interactions $N_c/6$, with N_d and N_c the number of defect and crystalline interactions within an assembly. We denote by ϵ_c and ϵ_d the energy of each contact. Both N_c and N_d depend on the radius of the assembly, which we denote by r . We compute the energy of a triangular slice, which corresponds to the subunits outlined in dark gray in Figure S3. The energy of a triangular slice then reads

$$E(r) = N_c(r)\epsilon_c + N_d(r)\epsilon_d \quad (4)$$

$3\epsilon_c - 2\epsilon_d$	+	+	+	-	-	-
ϵ_d	+	+	-	+	-	-
$\epsilon_c - \epsilon_d$	+	-	+	-	+	-
$\min_{r>0} (e_{\text{vortex}}(r))$	0	0	$r_v^* > 0$	$+\infty$	$+\infty$	$+\infty$
Self-limited vortex assembly	no	no	yes	no	no	no

Table S2. Determination of the regions of vortex assembly stability

We determine $N_c(r)$ and $N_d(r)$ from the drawings in Figure S3. The crystal interactions are colored green and the defect interactions are colored in blue. The number of crystal bonds scales like the surface of the assembly, r^2 and the number of defect bonds like its perimeter, which is proportional to r .

$$\frac{1}{6}N_c^{(\text{crystal})}(r) = 3r(r-1)/2 + 2r \quad (5)$$

$$\frac{1}{6}N_d^{(\text{crystal})}(r) = 0 \quad (6)$$

$$\frac{1}{6}N_c^{(\text{vortex})}(r) = 3r(r-1)/2 \quad (7)$$

$$\frac{1}{6}N_d^{(\text{vortex})}(r) = 2r - 1 \quad (8)$$

The total number of subunits in the crystal and vortex assembly are

$$N^{(\text{crystal})}(r) = 3r(r+1) + 1 \quad (9)$$

$$N^{(\text{vortex})}(r) = 3r(r+1) \quad (10)$$

We finally deduce the energy per subunit in a vortex assembly and a crystal.

$$e_{\text{crystal}}(r) = \frac{e_{\text{crystal}}(r)}{N^{(\text{crystal})}(r)} = \frac{(3r^2 + r)\epsilon_c}{r(r+1) + 1/3} \quad (11a)$$

$$e_{\text{vortex}}(r) = \frac{3r^2\epsilon_c + r(-3\epsilon_c + 4\epsilon_d) - 2\epsilon_d}{r(r+1)} \quad (11b)$$

Differentiating these energies and canceling their derivatives with r then gives the ground state for a selected geometry (vortex or crystal). This ground state depends on the binding energies ϵ_c and ϵ_d .

Energy Minimization

For each region of the parameter space (ϵ_c, ϵ_d) , we determine which assembly radius r_c^* and r_v^* minimizes the energies e_{crystal} and e_{vortex} . For this reason, we take the derivative of the energy per subunit, as shown in Eq. (11a) and Eq. (11b).

$$\partial_r e_{\text{crystal}}(r) = 3\epsilon_c \frac{6r^2 + 6r + 1}{(3r^2 + 3r + 1)^2} \quad (12a)$$

$$\partial_r e_{\text{vortex}}(r) = 2 \frac{(3\epsilon_c - 2\epsilon_d)r^2 + \epsilon_d(2r + 1)}{r^2(r+1)^2} \quad (12b)$$

The energy per subunit of the crystal is monotonic. Indeed, $\partial_r e_{\text{crystal}}(r)$ is positive for $\epsilon_c > 0$ and negative for $\epsilon_c < 0$. In the former case, the most stable crystal has radius 0: it is a monomer ($r_c^* = 0$, $e^{\text{crystal}} = 0$). In the latter, the most stable crystal has an infinite size ($r_c^* = \infty$, $e^{\text{crystal}} = 3\epsilon_c$).

The energy per subunit of the vortex assembly can have a minimum. We determine the value of this minimum, if it exists in each region of the parameter space, and summarize our results in Table S2. We find that the value of r minimizing $e_{\text{vortex}}(r)$ is positive and finite when $3\epsilon_c - 2\epsilon_d > 0$, $\epsilon_d < 0$, and $\epsilon_c > \epsilon_d$. r_v^* is obtained by finding the roots of the quadratic equation $\partial_r e_{\text{vortex}}(r) = 0$.

$$r_v^* = \frac{-\epsilon_d + \sqrt{\Delta}}{3\epsilon_c - 2\epsilon_d} \quad \text{and} \quad \Delta = -3\epsilon_d(\epsilon_c - \epsilon_d) \quad (13)$$

When choosing the parameters to run a numerical simulation, we select an integer target assembly radius r_v^* , and determine the corresponding energy ratio with equation Eq. (14), which is directly derived from Eq. (13).

$$\frac{\epsilon_c}{\epsilon_d} = \frac{2(r_v^*)^2 - 2(r_v^*) - 1}{3(r_v^*)^2} \quad (14)$$

In the following, we write $r_v^* = r^*$ to simplify the notations.

Phase Diagram Boundaries

In each region of the parameter space, we now determine which energy minimum of the vortex and crystal assemblies is smaller. This determines which assembly geometry is more stable. In cases where the energy minimum is at $r = +\infty$, we use the limit of the energy per subunit. Thus far, we know for each parameter regime the energy per subunit of the most stable crystal and of the most stable vortex assembly. Below, we compare those two energies in each parameter region. This enables us to construct the phase diagram of Fig. 2b of the main text.

- $\epsilon_c > 0$ and $\epsilon_d > 0$. Vortex assemblies are unstable: their energy per subunit increases with r , as shown in panel (c). It means that any crystalline assembly of more than one subunit is less favored than monomers of energy zero. Therefore, subunits do not self-assemble. This corresponds to the light green region in Fig. S4a.
- $\epsilon_c > 0$ and $\epsilon_d < 0$. Vortex assemblies are stable and their energy is minimum for $r = 1$. Indeed, we verify that $e_{\text{vortex}}(r = 1) < e_{\text{vortex}}(r > 1)$. The vortex energy then reads $e_{\text{vortex}}(r = 1) = \epsilon_d$. On the other end, crystal assemblies have a minimum energy for $r = 0$ and $e_{\text{crystal}}(r = 0) = 0$. Because $\epsilon_d < 0$, $e_{\text{vortex}}(r = 1) < e_{\text{crystal}}(r = 0)$. This means that vortex assemblies of radius 1 are the most stable geometry. This corresponds to the darker blue region in Fig. S4a: vortex assemblies of radius 1 are hexamers. The energy per subunit is minimum for $r = 1$ as shown in panel (b).
- $\epsilon_c < 0$, $\epsilon_d < 0$ and $3\epsilon_c - 2\epsilon_d > 0$. In this situation we compare $e_{\text{vortex}}(r_{\text{vortex}}^*)$ with $e_{\text{crystal}}(r = \infty) = 3\epsilon_c$.

$$e_{\text{vortex}}(r^*) - e_{\text{crystal}}(r = \infty) = \frac{3(r^*)^2\epsilon_c + r(-3\epsilon_c + 4\epsilon_d) - 2\epsilon_d}{r^*(r^* + 1)} - 3\epsilon_c = \frac{-2r^*(3\epsilon_c - 2\epsilon_d) - 2\epsilon_d}{r^*(r^* + 1)} \quad (15)$$

By substituting r^* in the numerator by its expression in Eq. (13), we get

$$e_{\text{vortex}}(r^*) - e_{\text{crystal}}(r = \infty) = \frac{-2\sqrt{\Delta}}{r^*(r^* + 1)} < 0. \quad (16)$$

Hence, vortex assemblies are more stable than crystals in this region, and have limited-size. This corresponds to the blue region labeled "vortex" in the phase diagram of Fig. S4a. The corresponding energy profile in panel (b) has a minimum for finite values of r .

- $\epsilon_c < 0$, $\epsilon_d < 0$, $3\epsilon_c - 2\epsilon_d < 0$ and $\epsilon_c - \epsilon_d > 0$. In this situation, both vortex assemblies and crystals are of infinite size. We thus compare $e_{\text{crystal}}(r = \infty)$ with $e_{\text{vortex}}(r = \infty)$. Since both expressions for the energies are equal to the order 1, we compare their values at the order $1/r$.

$$e_{\text{vortex}}(r = \infty) - e_{\text{crystal}}(r = \infty) = 3\epsilon_c + \frac{1}{r}(-3\epsilon_c + 4\epsilon_d) - 3\epsilon_c - \frac{1}{r}\epsilon_c + \mathcal{O}\left(\frac{1}{r^2}\right) \quad (17)$$

$$= \frac{4}{r}(\epsilon_d - \epsilon_c) + \mathcal{O}\left(\frac{1}{r^2}\right) \quad (18)$$

$$< 0 \quad (19)$$

The vortex assemblies are more stable than the crystals assemblies in this region. This corresponds to the light blue region in Fig. S4a. There, the energy per subunit decreases with r as shown in panel (b).

- $\epsilon_c < 0$ and $\epsilon_c - \epsilon_d < 0$. When $\epsilon_d < 0$, vortex assemblies are stable and of infinite size, and the previous calculations hold. However, we now see from Eq. (18) that crystals are more stable than vortex assemblies. When $\epsilon_d > 0$, vortex assemblies are unstable (their energy increases with r) and infinite crystals are more stable. Those two cases correspond to the dark green region in Fig. S4a. The energy profile is that of panel (c): it decreases with r .

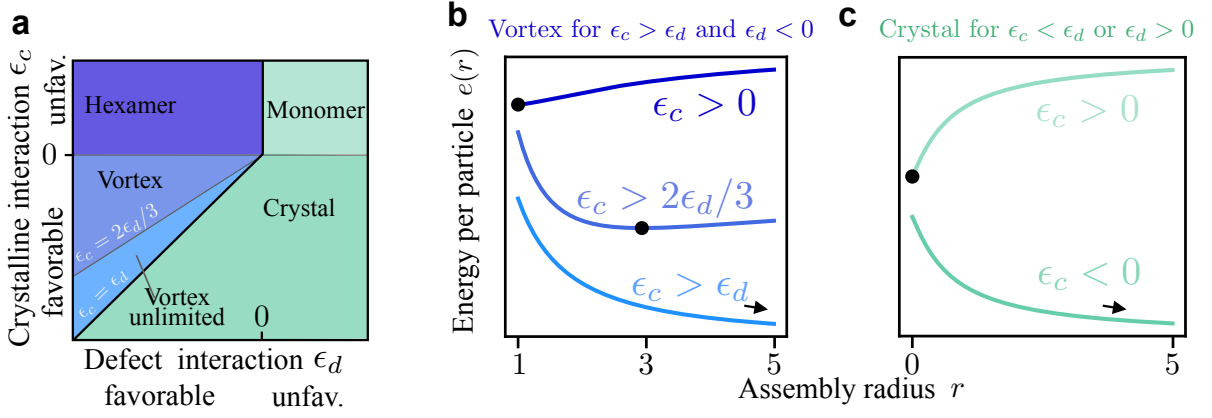


Figure S4. **Favorable defects result in vortex assemblies of finite equilibrium sizes for weakly attractive crystalline interactions.** (a) $e_{\text{vortex}}(r)$ is lower than $e_{\text{crystal}}(r)$ in the green regions of the phase diagram. (b) The vortex assembly energy is minimum for a finite radius larger than 1 in the region $\epsilon_d < 0$ and $0 > \epsilon_c > 2\epsilon_d/3$. (c) There is no such non-trivial minimum for the crystal energy.

Favored Assembly Size

In the previous subsections, we established a relation between the assembly size r^* that minimizes the vortex assembly energy, and the specific ratio of crystalline and defect interaction energies of the subunit Eq. (14). However, inverting this formula can lead to non-integer favored assembly sizes r^* , which are not accounted for by our model of idealized geometry. Here, we explicitly determine, for any energy ratio, the most favored integer assembly radius of a vortex assembly.

We assume that the assembly is perfectly symmetric, and that all its domains have the same integer size r . For a fixed energy ratio ϵ_c/ϵ_d , the assembly size r^* which minimizes the energy satisfies

$$e_{\text{vortex}}(r^* - 1) > e^{(\text{vortex})}(r^*) \quad (20a)$$

$$e_{\text{vortex}}(r^* + 1) > e^{(\text{vortex})}(r^*), \quad (20b)$$

the expression for $e_{\text{vortex}}(r)$ is given in Eq. (11b).

From Eq. (14), we observe that r^* increases with increasing ϵ_c/ϵ_d . We therefore need to solve only one of the two equations of Eq. (20). We deduce the following dependence for the integer radius r^* on ϵ_c/ϵ_d that minimizes the assembly energy.

$$r^* = 1 + \text{floor} \left(\frac{2}{2 - 3\epsilon_c/\epsilon_d} \right) \quad (21)$$

We use Eq. (21) for the theoretical curve of Fig. 3h of the main text. Inverting this expression now allows us to determine $(\epsilon_c/\epsilon_d)_{\text{lim}}(r^*)$, the energy ratio for which assemblies of size r^* become more favorable than those of size $r^* - 1$.

$$(\epsilon_c/\epsilon_d)_{\text{lim}}(r^*) = \frac{2r^* - 2}{3r^* - 1} \quad (22)$$

These ratios determine the boundary between the stability region of vortex assemblies of different sizes. They are plotted in the phase diagram of Fig. 2b of the main text as gray lines. Therefore, these formulas now provide a fully consistent prediction of idealized vortex assembly sizes for any subunit interactions ϵ_d and ϵ_c .

2 Generalization of the Defect Engineering Principle

Changing the subunit interaction rules makes it possible to obtain different types of assemblies. In particular, we can vary the number of disclinations in the vortex assemblies, or obtain assemblies that are unlimited in one dimension (fibers) or two dimensions (patterned bulks). Below, we present the calculations used to obtain the energy per subunit and the dependence of the most energetically favored radius on ϵ_c/ϵ_d for each type of assembly presented in Fig. 4 of the main text.

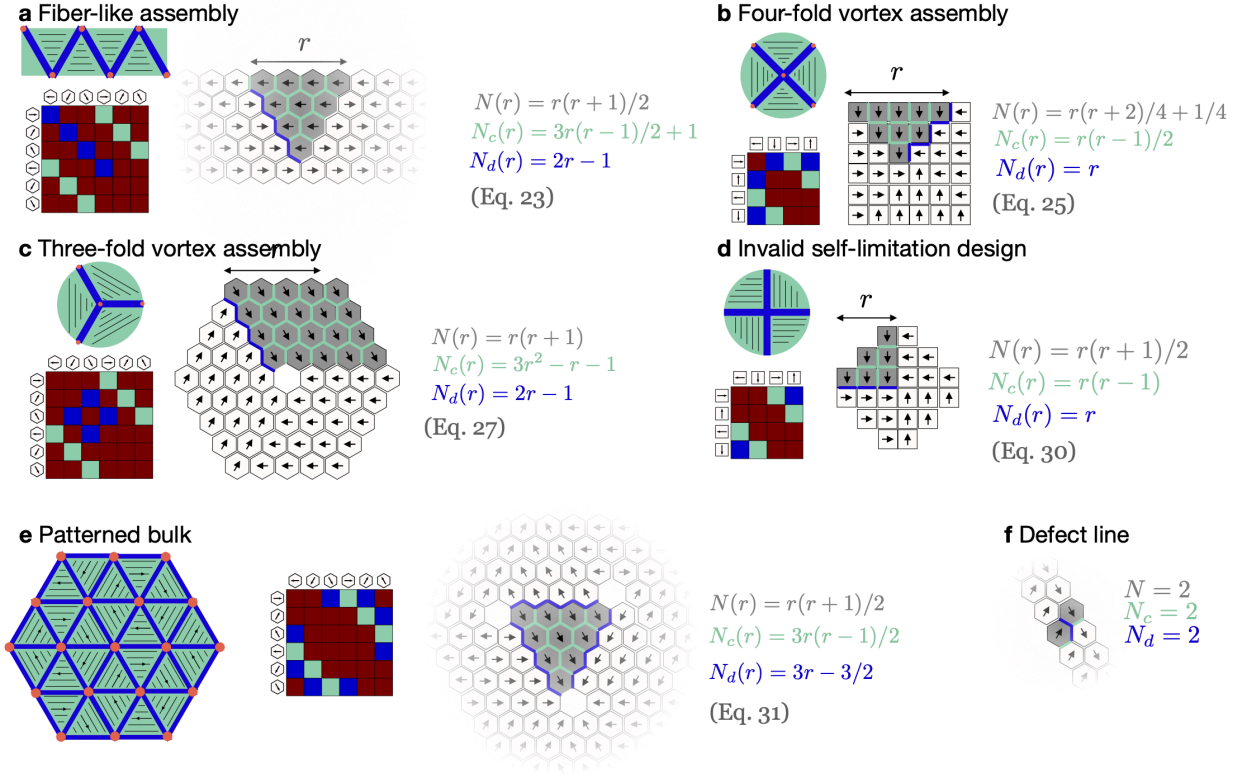


Figure S5. **Idealized geometry of fibers, vortex assemblies and bulks.** For each assembly type, we show the assembly schematic, all the possible interactions in a contact map using the color coding of Fig. S3, and an idealized assembly. We count the total number of subunits and the number of crystalline and defect contacts for the triangular slice of size r colored in gray. We detail these countings for a fiber-like assembly (a), a four-fold (b) and three-fold (c) vortex assembly, an invalid self-limitation design (d) and a patterned bulk (e). In (f) we show the energy per subunit in a fiber defect.

Fiber-like Assembly

We compute the energy per subunit of fiber-like assemblies shown in Fig. 4a-c of the main text and demonstrate that they can be stable at a finite width. In this geometry, the triangular crystalline regions are in contact through defect interactions that reverse the subunits' orientation. As before, we compute the energy per subunit by determining the number of crystalline and defect interactions as a function of the crystalline domain size r , as shown in the inset of Fig 4b of the main text. For this calculation, we neglect the energy contribution from the ends of the fibrous assembly: we compute the energy of an infinitely long fiber.

$$N(r) = r(r+1)/2 \quad (23a)$$

$$N_c(r) = 3r(r-1)/2 + 1 \quad (23b)$$

$$N_d(r) = 2r - 1 \quad (23c)$$

$$e_{\text{fiber}}(r, \epsilon_c, \epsilon_d) = \frac{N_c(r)\epsilon_c + N_d(r)\epsilon_d}{N(r)} = \frac{3\epsilon_c r^2 + r(4\epsilon_d - 3\epsilon_c) + 2\epsilon_c - 2\epsilon_d}{r(r+1)}. \quad (23d)$$

Similar calculations to those of Section S31 allow to build the phase diagram of Fig. 4b of the main text from the expression of e_{fiber} . This energy possesses a finite minimum r^* under the conditions that $\epsilon_c < 0$, $\epsilon_d < 0$, and $\epsilon_c/\epsilon_d < 2/3$. In particular, the assembly size at equilibrium r^* is related to the interaction energy ratio by

$$\frac{\epsilon_c}{\epsilon_d} = \frac{2(r^*)^2 - 2r^* - 1}{3(r^*)^2 - 2r^* - 1} \quad (24)$$

For the simulations in Fig. 4c of the main text, we choose the energy ratio corresponding to $r^* = 2, 4$ or 6 .

Four-fold Vortex Assembly

Here, we compute the energy per subunit for four-fold vortex assemblies and show that they can have an energy minimum at a finite size r . We consider square subunits, as in the schematic of Fig. S5b, or in Fig. 4g of the main text. We compute the energy per subunit:

$$N(r) = r(r+2)/4 + 1/4 \quad (25a)$$

$$N_c(r) = r(r-1)/2 \quad (25b)$$

$$N_d(r) = r \quad (25c)$$

$$e_4(r, \epsilon_c, \epsilon_d) = 4 \frac{N_c(r)\epsilon_c + N_d(r)\epsilon_d}{4N(r)} = 2 \frac{\epsilon_c r^2 + r(2\epsilon_d - \epsilon_c)}{(r+1)^2} \quad (25d)$$

This energy exhibits a finite minimum r^* under the conditions that $\epsilon_c < 0$, $\epsilon_d < 0$ and $\epsilon_c/\epsilon_d < 2/3$. In particular, the assembly size at equilibrium r^* relates to the interaction energy ratio as

$$\frac{\epsilon_c}{\epsilon_d} = \frac{2r^* - 1}{3r^* - 1}. \quad (26)$$

For the simulations in Fig. 4c of the main text, we fix the subunit binding energies ϵ_c and ϵ_d such that their ratio matches $r^* = 2, 4$ or 6 .

Three-fold Vortex Assembly

Here, we compute the energy per subunit of three-fold vortex assemblies (Fig. 4f of the main text) and show that they are not stable at finite sizes: individual defect lines are more stable than the size-limited three-fold vortex assembly. We design the defect interactions of the hexagonal subunits such that the angle between the orientations of two crystalline domains is $2\pi/3$. Such subunits should assemble in a three-fold vortex assembly, provided there are no assembly geometries that are more favored. We compute the energy per subunit in this hypothetical three-fold vortex assembly, following the schematic of Fig. S5c:

$$N(r) = r(r+1) \quad (27a)$$

$$N_c(r) = 3r^2 - 3r - 1 \quad (27b)$$

$$N_d(r) = 2r - 1 \quad (27c)$$

$$e_3(r, \epsilon_c, \epsilon_d) = 3 \frac{N_c(r)\epsilon_c + N_d(r)\epsilon_d}{3N(r)} = \frac{3\epsilon_c r^2 - r(2\epsilon_d - \epsilon_c) - \epsilon_c - \epsilon_d}{r(r+1)} \quad (27d)$$

This energy e_3 has a finite minimum r^* under the conditions $\epsilon_c < 0$, $\epsilon_d < 0$ and $\epsilon_c/\epsilon_d < 0.5$. In particular, the assembly size at equilibrium r^* relates to the interaction energy ratio as

$$\frac{\epsilon_c}{\epsilon_d} = \frac{2(r^*)^2 - 2r^* - 1}{4(r^*)^2 + 2r^* + 1} = \alpha(r^*). \quad (28)$$

We now consider the parameter regime where three-fold vortex assemblies of size r^* are favored, and we compare the energy of a hypothetical self-limited three-fold vortex assembly with that of individual defect lines. We first compute the energy of an assembly of radius r^* : we replace r with r^* and ϵ_d by $\epsilon_c/\alpha(r^*)$ in Eq. (27d). On the other hand, in an individual defect line, each subunit realizes one defect and one crystalline interaction, as shown in Fig. S5f. The energy per subunit of individual defect lines is therefore $\epsilon_c + \epsilon_d = \epsilon_c + \epsilon_c/\alpha(r^*)$. In Eq. (29), we compute the energy difference of a subunit within a three-fold vortex assembly and within a thin defect line. We demonstrate that it is positive, meaning that defect fibers are more stable.

$$e_3(r^*, \epsilon_c, \epsilon_c/\alpha(r^*)) - (\epsilon_c + \epsilon_c/\alpha(r^*)) = \frac{3 - 6r^*}{2(r^*)^2 - 2r^* - 1} \epsilon_c \quad (29)$$

This quantity is positive for $r^* > 1/2$, which means that a three-fold vortex assembly of finite radius is always less stable than a fiber. This explains the formation of individual defect line for $\frac{\epsilon_c}{\epsilon_d} < 0.5$ observed in the simulation in Fig. 4f of the main text. In the regime where $\frac{\epsilon_c}{\epsilon_d} > 0.5$ however, e_3 is minimum at $r \rightarrow \infty$ and $e_3(r \rightarrow \infty) = 3\epsilon_c < \epsilon_c + \epsilon_d$. Therefore, the infinite three-fold vortex assembly is more stable than the individual defect line in that regime, as shown in Fig. 4f of the main text.

Invalid Self-Limited Design

Here, we show that the four-fold vortex assembly, where the defects are parallel to the subunits' orientation, (Fig. 4h of the main text) does not display any energy minima for finite sizes. As in Section S32, we use square subunits for this design (see Fig. S5d).

$$N(r) = r(r+1)/2 \quad (30a)$$

$$N_c(r) = r(r-1) \quad (30b)$$

$$N_d(r) = r \quad (30c)$$

$$e_i(r, \epsilon_c, \epsilon_d) = 4 \frac{N_c(r)\epsilon_c + N_d(r)\epsilon_d}{4N(r)} = 2 \frac{\epsilon_c r - (\epsilon_d - \epsilon_c)}{r+1} \quad (30d)$$

This energy does not have a minimum for finite and positive r . It increases with increasing r if $\epsilon_c/\epsilon_d < 0.5$, and it decreases with increasing r otherwise.

Patterned Bulk

Here, we compute the energy per subunit in a patterned bulk, as shown in Fig. 4e of the main text. We show that patterned bulks have an energy minimum for finite-sized triangular domains. To obtain patterned bulks, we start from the interactions leading to the 6-fold vortex assembly, and add an interaction allowing those assemblies to favorably bind. Each triangular slice now has three defect lines, shared between two slices. The energy per subunit of such triangle, calculated following the schematic of Fig. S5e, reads

$$N(r) = r(r+1)/2 \quad (31a)$$

$$N_c(r) = 3r(r-1)/2 \quad (31b)$$

$$N_d(r) = 3(2r-1)/2 \quad (31c)$$

$$e_p(r, \epsilon_c, \epsilon_d) = \frac{N_c(r)\epsilon_c + N_d(r)\epsilon_d}{N(r)} = \frac{3\epsilon_c r^2 - r(3\epsilon_c - 6\epsilon_c) - 3\epsilon_d}{r(r+1)}. \quad (31d)$$

This energy exhibits a finite minimum r^* under the conditions that $\epsilon_c < 0$, $\epsilon_d < 0$ and $\epsilon_c/\epsilon_d < 1$. In particular, to obtain the domain size r^* in the patterned assembly, the energy ratio is

$$\frac{\epsilon_c}{\epsilon_d} = \frac{2(r^*)^2 - 2r^* - 1}{2r^*}. \quad (32)$$

For the simulations in Fig. 4e of the main text, we fix the subunit binding energies ϵ_c and ϵ_d such that their ratio corresponds to $r^* = 2, 4$ or 6 .

3 Entropic Effect Influences the Equilibrium Size Distribution

The phase diagram established in the Section S31 allows us to predict the type of assembly the subunits will assemble into and the size of the assembly at equilibrium: this was determined by minimizing the energy per subunit. However, both experiments and simulations are performed at finite temperature, and we here discuss the influence of entropic effects to predict the size distribution of the assemblies. In particular, we emphasize the need to account for grain boundaries that are longer than the assembly radius. We also find that the most likely assembly radius is always the most favored one in the temperature range that is relevant for the simulation and experiments. The calculations derived in this section allow to plot the theoretical prediction for the assembly size distribution shown in Fig. 2d of the main text.

Branches Energetic Contribution

In the simulation results presented in Fig. 2c of the main text, we see that some vortex assemblies deviate from the idealized prediction of the previous subsection. In particular, for low interaction energy ratio ϵ_c/ϵ_d , some grain boundaries are longer than the assembly size r . In this section, we refer to these extended grain boundaries as

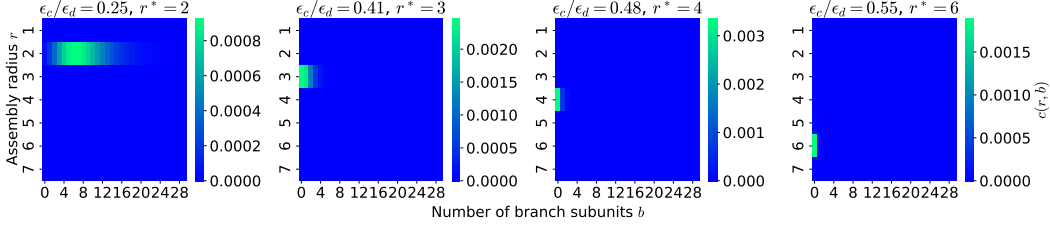


Figure S6. **Branches are unfavored for equilibrium radius larger than 2.** (a) We parametrize the assembly by its core size r and the number of subunits in branches (colored in red) b . (b) For the interaction energies as in the main text, the distribution of assembly radius and branches size is peaked around the equilibrium radius r^* and $b = 0$, except for the case $r^* = 2$, for which branches are energetically favored, and their size is limited entropically.

branches. We complete our theory and parametrize the energy per subunit in an assembly by its radius r , and the number of subunits in a branch. We conclude that assemblies with branches are energetically favored only for small assembly sizes.

We denote by b the number of subunits within branches. They are colored in red in Fig. S1b. The energy per subunit in a defect-limited assembly is now parameterized by both r and b . We modify the total number of subunits in the assembly as follows

$$N(r, b) = 3r(r + 1) + b. \quad (33)$$

When a subunit is added to form a branch, it adds one surface interaction and one crystalline interaction. We therefore modify N_c and N_d as follows

$$N_c(r, b) = 6 \times (3r(r - 1)/2) + b \quad (34a)$$

$$N_d(r, b) = 6 \times (2r - 1) + b. \quad (34b)$$

The energy per subunit in a defect-limited assembly now reads

$$e_{\text{vortex}}(r, b) = \frac{9r(r - 1)\epsilon_c + b\epsilon_c + 6(2r - 1)\epsilon_d + b\epsilon_d}{3r(r + 1) + b}. \quad (35)$$

We can differentiate this expression with b as follows

$$\frac{\partial e_{\text{vortex}}(r, b)}{\partial b} = \frac{3(r - 2)(r(\epsilon_d - 2\epsilon_c) - \epsilon_d)}{(3r(r + 1) + b)^2}. \quad (36)$$

We notice that the sign of this derivative is independent of b : the branches are either unfavored ($b^* = 0$), or they are favored, and their length is not determined by an energy minimum, but by entropic constraints. We express the sign of $\partial_b e_{\text{vortex}}(r, b)$ as follows

$$\partial_b e_{\text{vortex}}(r, b) > 0 \Rightarrow \epsilon_d(r - 2)\left(r\left(1 - 2\frac{\epsilon_c}{\epsilon_d}\right) - 1\right) > 0 \quad (37a)$$

$$\Rightarrow (r - 2)\left(r\left(1 - 2\frac{\epsilon_c}{\epsilon_d}\right) - 1\right) < 0. \quad (37b)$$

If we choose $r = r^*$ and $\frac{\epsilon_c}{\epsilon_d}$ determined by r^* through Eq. (14), the quantity of Eq. (37)b is always negative, except for $r^* = 2$ where it is null. Therefore, branches are energetically unfavored, except for a specific value of ϵ_c/ϵ_d for which vortex assemblies of size 2 are favored. This explains the presence of branches in the numerical simulation shown in Fig. 2c of the main text.

Assembly Size Distribution

So far, we used our model to relate the interaction energy ratio to the assembly size at equilibrium. However, experiments and simulation are performed at finite temperature, and the minimum of the energy profile of a vortex assembly is shallow, such that assemblies of larger or smaller radii than r^* , or assemblies with branches, can be observed. Here, we determine the expected distribution of assembly sizes, and find that they are peaked around the

thermodynamic minimum. In this derivation, we account for the extended grain boundaries (branches) introduced in the previous subsection.

We consider an ideal gas of assemblies where there are $m(r, b)$ assemblies of radius r with b subunits in the branches. Without interactions between assemblies, the partition function of the total system Z is the product of the partition function of the individual assemblies $z(r, b)$, weighted by their number of configurations.

$$Z = \prod_{r,b} \frac{1}{m(r, b)!} [z(r, b)]^{m(r, b)} \quad (38)$$

The partition function of an individual assembly counts all the possible positions of the assembly in the system. There are N_{sites} possible positions. It reads

$$z(r, b) = N_{\text{sites}} e^{-\beta N(r, b) e_{\text{vortex}}(r, b)}, \quad (39)$$

where $e_{\text{vortex}}(r, b)$ is the energy per subunit in a vortex assembly (Eq. (35)), $N(r, b)$ is the number of subunits in the vortex assembly (Eq. (33)), and $\beta = k_B T$ is the inverse temperature. With the Stirling approximation for the factorial, we obtain an expression for the free energy

$$F = -\frac{1}{\beta} \ln Z = \sum_{r,b} \left[-\frac{1}{\beta} m(r, b) \ln \frac{e^{N_{\text{sites}}} m(r, b)}{m(r, b)!} + m(r, b) N(r, b) e_{\text{vortex}}(r, b) \right]. \quad (40)$$

If we now introduce the concentration of clusters of size $N(r, b)$, $c(r, b) = m(r, b)/N_{\text{sites}}$, we obtain for the free energy per unit volume

$$f = \frac{F}{N_{\text{sites}}} = \sum_{r,b} N(r, b) c(r, b) \left[\frac{1}{N(r, b) \beta} (\ln c(r, b) - 1) + e_{\text{vortex}}(r, b) \right]. \quad (41)$$

The total concentration of subunits being fixed, we differentiate f for a fixed value of $\sum_{r,b} N(r, b) c(r, b)$. The thermodynamic potential associated to this constraint is μ . We compute the derivative of f with respect to $c(r, b)$ with this constraint, and impose that it vanishes at equilibrium.

$$\frac{\partial}{\partial c(r, b)} [f - \mu \sum_{r,b} N(r, b) c(r, b)] = \frac{1}{\beta} (\ln c(r, b) + N(r, b) (e_{\text{vortex}}(r, b) - \mu)) = 0 \quad (42)$$

We deduce the following expression for $c(r, b)$

$$c(r, b) = e^{-\beta N(r, b) (e_{\text{vortex}}(r, b) - \mu)}. \quad (43)$$

If $c_0 = c(0, 0)$ is the monomer concentration in the system, and the energy of a monomer is $e(0, 0) = 0$, the concentration of assemblies of radius r with b branch subunit is

$$c(r, b) = \left(c_0 e^{-\beta e_{\text{vortex}}(r, b)} \right)^{N(r, b)}. \quad (44)$$

This calculations so far assumed that there is only one configuration of assembly of radius r with b branch subunits. However, the subunits within the branches can be distributed in different ways without changing the energy of the assembly. For instance, if $b = 5$, each of the 6 branches of the assembly can be respectively of length 2, 2, 1, 0, 0 and 0, or 1, 0, 1, 0, 3 and 0. There are $\binom{b+5}{5}$ ways of distributing b subunits among 6 branches. Indeed, choosing how to distribute the subunits within the branches is similar to placing 5 separations (that separate between subunits belonging to different branches) in an array of b subunits. Taking this into account, the distribution of branch and assembly size reads

$$c(r, b) = \binom{b+5}{5} \left(c_0 e^{-\beta (e_{\text{vortex}}(r, b))} \right)^{N(r, b)}. \quad (45)$$

Finally, we determine c_0 numerically by solving

$$\sum_{r,b} N(r, b) c(r, b) = \frac{N_{\text{subunits}}}{N_{\text{sites}}}. \quad (46)$$

The distribution in Fig. S6 is peaked around the energy minimum, thus suggesting that entropic effects are negligible, except in the case $r^* = 2$, where the branches are favored. We also deduce from Eq. (45) the distribution of branches, or radii, individually, by summing over the other variable as follows:

$$c_r(r) = \sum_b c(r, b) \quad (47a)$$

$$c_b(b) = \sum_r c(r, b). \quad (47b)$$

Finally, we determine the theoretical cumulative probability distributions for the assembly radius and branch size as follows

$$P_r^{\text{theory}}(k \leq r) = \frac{\sum_{k \leq r} c_r(k)}{\sum_{k \leq L} c_r(k)} \quad (48a)$$

$$P_b^{\text{theory}}(p \leq b) = \frac{\sum_{p \leq b} c_b(p)}{\sum_{p \leq L} c_b(p)}. \quad (48b)$$

Both sums run on values of r and b up to the system size $L = 40$. $P_r^{\text{theory}}(k \leq r)$ is plotted in Fig. 2d of the main text and directly compared to the same quantity measured in the simulation, defined in Eq. (2).

S4 Enhanced Theory–Simulation Agreement via Extended Annealing

In Fig. 2d and 3h of the main text, we observe a small discrepancy between the predicted and simulated assembly sizes. In this section, we show that increasing the annealing time steadily improves agreement with theory, highlighting the reliability of the prediction despite computational constraints.

We vary the annealing time A for the binding energy ratios ϵ_c/ϵ_d discussed in the main text, and track how the average assembly radius and the distributions of radii and branch sizes evolve. As shown in Fig. S7a, the assembly radius converges quickly toward the predicted equilibrium value r^* for $r^* = 2$ and $r^* = 3$. For larger target sizes ($r^* = 4$ and $r^* = 6$), equilibration requires significantly more computational effort, explaining the small discrepancy observed in Fig. 3h.

Fig. S7b and Fig. S7c display the distributions of assembly radii and branch sizes across different annealing protocols, compared to the theoretical predictions derived from Eq. (48). The theoretical distributions assume integer values for k and p , while the simulations account for all observed values, whether integer or not. In Fig. S7b and Fig. S7c, we show the measured and predicted radius and branch size distributions. For radius $r^* = 4$ and $r^* = 6$, we observe more assemblies of radii $r = 3$ and $r = 5$ and 6 , respectively, than predicted.

This deviation can be attributed to two factors. First, as shown in Fig. S4, the energy landscape around r^* is shallow, leading to a high density of near-degenerate states. Second, vortex assemblies nucleate easily: their six central subunits interact only through highly favored defect interactions. If too many such assemblies nucleate early, some remain small due to the finite number of subunits available.

The mismatch in predicted and measured branch sizes for larger assemblies ($r^* > 3$) stems from a difference in geometry. While small assemblies often follow the ideal hexagonal-with-branches structure described in Fig. S1b, larger assemblies tend to form irregular crystalline domains, as seen in the top-right assembly of the $r^* = 6$ panel in Fig. 2c. In such cases, applying Eq. (1) yields a nonzero branch count even when no actual branches are present, resulting in a systematic overestimation of branch numbers in Fig. S7c.

Our results demonstrate a clear trend: longer annealing times lead to closer agreement between simulated and theoretical assembly properties. While full convergence for larger assemblies remains computationally demanding, the consistent improvement supports the accuracy of the theoretical model. The remaining differences, especially in branch size, are explained by the geometry of the assemblies seen in simulations.

S5 Geometrical Considerations

Here we use theory to demonstrate constraints on the morphology of the assemblies discussed in Figs. 2 and 3 of the main text. In Sec. S5.1, we map the discrete description of the orientations of our subunits to an equivalent field formalism. We then express the assemblies' defect energy in this formalism in Sec. S5.2, then derive the geometrical considerations discussed in the main text in Sec. S5.3. Finally in Sec. S5.4 we demonstrate some constraints on the

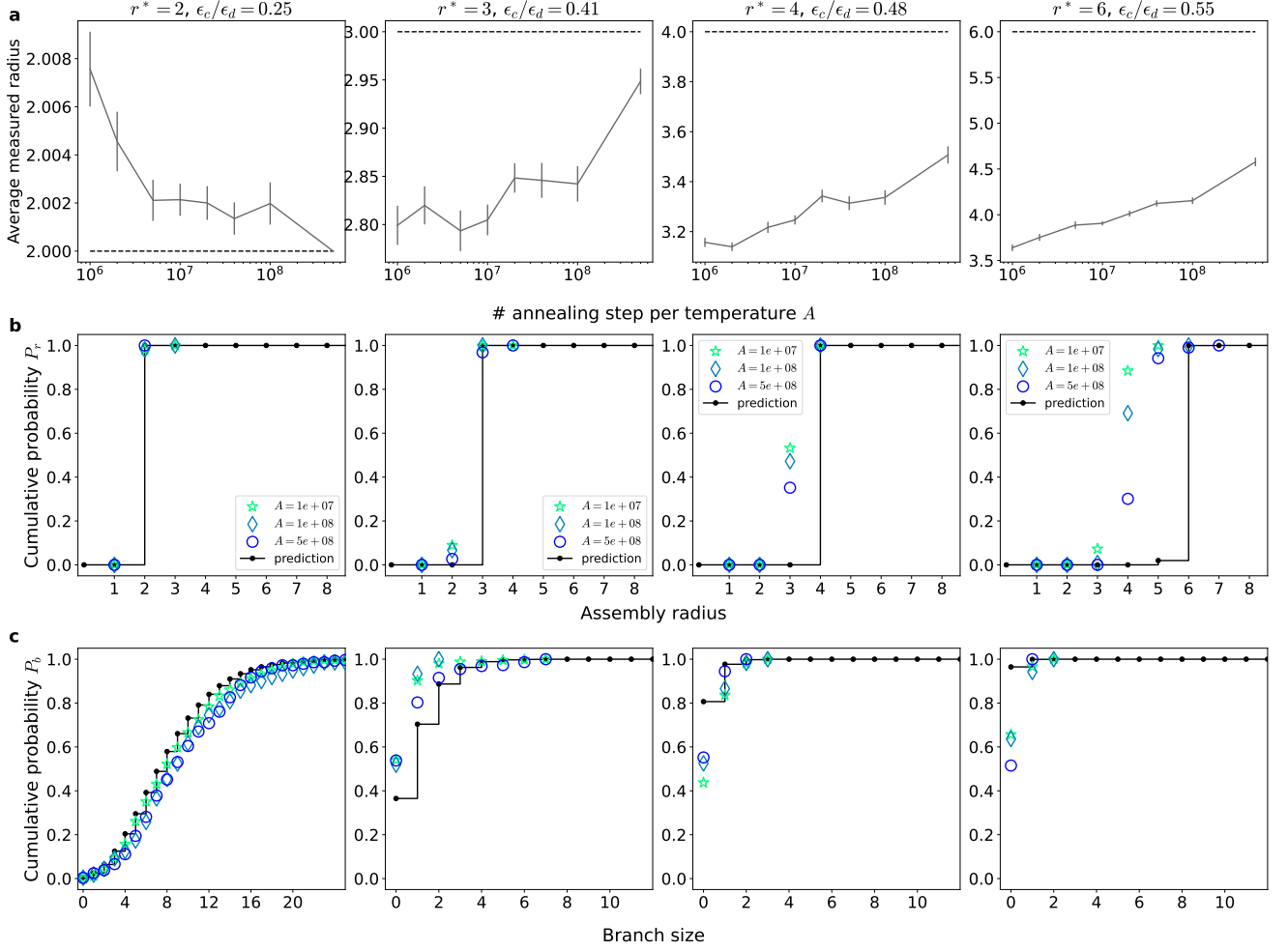


Figure S7. **Convergence of simulated assembly size toward theoretical prediction with increasing annealing time** (a) The assembly radius increases with the annealing time for the larger assemblies. (b) When well equilibrated, assembly radius distributions are well predicted by the theory. (c) Branch size distribution are qualitatively well predicted by our theory.

topological nature of the defects contained within our assemblies, and discuss why they favor vortex assemblies to the exclusion of assemblies with other winding numbers.

For the purposes of this section it is convenient to use a different convention for our interaction energies than that described in the main text. The energy used in the main text reads

$$E = N_c \epsilon_c + N_d \epsilon_d, \quad (49)$$

where N_c and N_d respectively denote the number of crystalline and defect interfaces, and ϵ_c and ϵ_d their energies. We also introduce the number S of interfaces between a subunit and an empty site (represented in orange in all figures). Denoting the total number of subunits in our system as N , and recalling that each subunit has six sides, we can write the total number of sides in our system as $6N$. That number is moreover also equal to $2N_c + 2N_d + S$. Subtracting the constant $3N$ from Eq. (49) and using this equality, we obtain the physically equivalent form

$$E = N_d(\epsilon_d - \epsilon_c) - S \frac{\epsilon_c}{2}, \quad (50)$$

which boils down to assigning an energy 0 to crystalline interfaces, an energy $\epsilon_d - \epsilon_c$ to defect interfaces and an energy $-\epsilon_c/2$ to interfaces at the surface of the assembly. We adopt this point of view throughout this section.

1 Interpolation of a Field Theory

Consider a connected assembly of oriented hexagonal subunits on a triangular lattice. In this assembly, interfaces between neighboring subunits are either of the crystalline type or of the defect type illustrated in Fig. 2a of the main text. We denote the length of a subunit edge by a .

We define an orientation field $\tilde{\theta}(\mathbf{x})$ at every point \mathbf{x} within the assembly through the procedure illustrated in Fig. S8a. In the procedure, points within a subunit are assigned the orientation of the subunit unless they are within a small boundary region of width d centered around a defect interface. Within this boundary region, the field instead interpolates between the orientations on either side by rotating by an angle $\pi/3$. We consider the $d \ll a$ limit, and within it the detailed form of the interpolating function does not matter for our discussion. We however assume that it is designed in such a way that (i) the function $\tilde{\theta}(\mathbf{x})$ is differentiable everywhere within the assembly and (ii) That the field monotonically interpolates between the orientation of two neighboring subunits while choosing the shortest path on the unit circle to do so. For instance, we assume that the interpolation between $\tilde{\theta} = 0$ and $\tilde{\theta} = \pi/3$ proceeds through a monotonic increase over the interval $0 \leq \tilde{\theta} \leq \pi/3$ as opposed to a decrease over $2\pi \geq \tilde{\theta} \geq \pi/3$.

Within this continuous formalism, we denote the set of points belonging to the assembly (*i.e.*, located within any of the hexagonal subunits of the assembly) as Ω . The orientation within Ω can be equivalently parametrized by any field $\theta(\mathbf{x}) = \tilde{\theta}(\mathbf{x}) + \theta_0$, where θ_0 is an arbitrary constant. In the following we choose an offset $\theta_0 = -2\pi/3$ compared to the convention of the main text. We define the unitary orientation vector field as

$$\hat{\mathbf{s}}(\mathbf{x}) = \begin{pmatrix} \cos \theta(\mathbf{x}) \\ \sin \theta(\mathbf{x}) \end{pmatrix}. \quad (51)$$

In this new convention, the unit vector field $\hat{\mathbf{s}}$ is tangent to the overall direction of the outer boundary of the ideal vortex assembly shown in the inset of Fig. 2b of the main text.

2 Continuum Expression for the Defect Energy

Using our orientation field formalism, we propose to write the defect energy of the assembly as

$$E_d = \frac{2(\epsilon_d - \epsilon_c)}{\sqrt{3}a} \iint_{\Omega} \nabla \times \hat{\mathbf{s}} \, dA, \quad (52)$$

where dA denotes the area element. To verify that this expression matches the discrete definition of the main text to lowest order in d/a , we first note that the value of its integrand vanishes everywhere except within our boundary regions of thickness d . We then compute its value for the representative portion of grain boundary represented in Fig. S8b. We denote the thus-defined domain by ω and use Stokes' theorem:

$$E_d = \frac{2(\epsilon_d - \epsilon_c)}{\sqrt{3}a} \iint_{\omega} \nabla \times \hat{\mathbf{s}} \, dA = \frac{2(\epsilon_d - \epsilon_c)}{\sqrt{3}} \oint_{\partial\omega} \hat{\mathbf{s}} \cdot \hat{\mathbf{t}} \, dl, \quad (53)$$

where $\hat{\mathbf{t}}$ is the tangent vector to domain ω and dl is the associated length element. To lowest order in d , the line integral of Eq. (53) can be approximated by a sum of straight segments which we each label by i , yielding

$$E_d = \frac{2(\epsilon_d - \epsilon_c)}{\sqrt{3}a} \sum_i a \hat{\mathbf{s}}_i \cdot \hat{\mathbf{t}}_i \quad (54)$$

The example of Fig. S8b displays the two possible types of defect interfaces associated with our design. It yields $\hat{\mathbf{s}}_1 \cdot \hat{\mathbf{t}}_1 = \hat{\mathbf{s}}_3 \cdot \hat{\mathbf{t}}_3 = 0$ and $\hat{\mathbf{s}}_2 \cdot \hat{\mathbf{t}}_2 = \hat{\mathbf{s}}_4 \cdot \hat{\mathbf{t}}_4 = \sqrt{3}/2$. Combining this result with Eq. (54) implies that each interface brings a contribution $\epsilon_d - \epsilon_c$ to the defect energy, thus validating the expression proposed in Eq. (52).

3 Upper Bound on the Number of Defect Interactions

We now use the expression of Eq. (52) to establish a bound on the assembly defect energy. Since as discussed in Eq. (50) this energy can alternatively be written as $E_d = N_d(\epsilon_d - \epsilon_c)$, we can write

$$N_d = \frac{2}{\sqrt{3}a} \iint_{\Omega} \nabla \times \hat{\mathbf{s}} \, dA = \frac{2}{\sqrt{3}a} \oint_{\partial\Omega} \hat{\mathbf{s}} \cdot \hat{\mathbf{t}} \, dl, \quad (55)$$

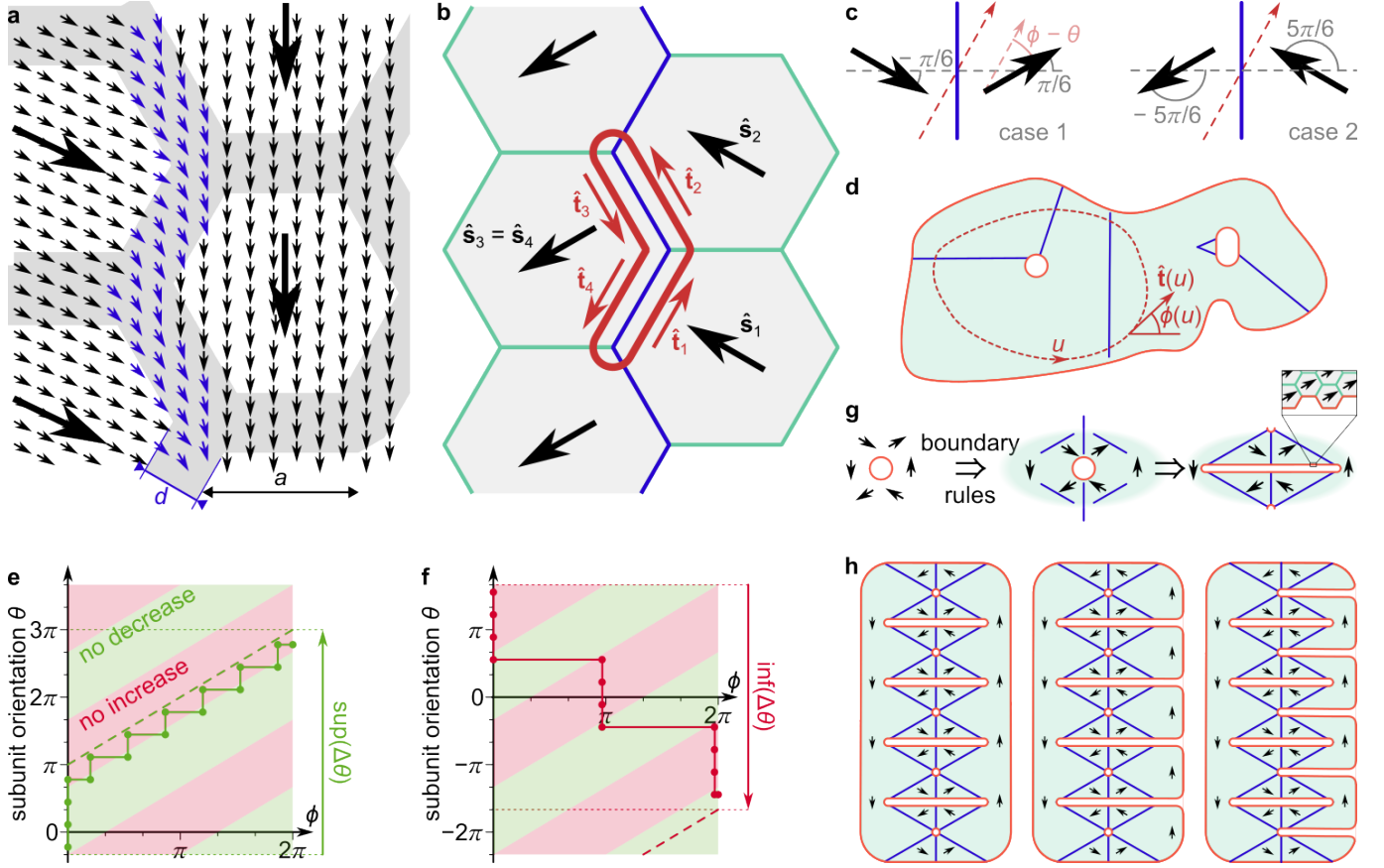


Figure S8. **Geometrical constraints on the presence of defect interactions in an assembly.** **a.** Interpolation of a smooth orientation field $\hat{\theta}(\mathbf{x})$ (*small arrows*) from the subunit orientations (*large black arrows*, with the orientation convention of the main text). The arrows within a neighborhood d of a defect interaction interpolate between the subunit orientations on either side of it (*dark blue*). **b.** Integration domain ω (*dark red*) used to relate the discrete and continuum expressions for the defect energy. Here the subunit orientation is pictured with the convention introduced in Sec. S51 **c.** Coarse-graining the corrugated defect boundary of panel **b** to a straight line produces two possible cases for the crossing of this boundary (*dark blue*) by a locally straight, oriented curve (*dashed red arrow*). Cases 1 and 2 respectively correspond to situations where the boundary of panel **b** is crossed from right to left, and from left to right. The dashed gray line materializes the normal to the boundary, and the light red angle highlights the angle $\phi - \theta$ between the orientation of the tangent to the curve and the orientation of the subunits in one of the crystalline domains. **d.** Construction of a convex loop (dashed red line) used to evaluate the winding number of the subunit orientation. Blue lines show the coarse-grained straight grain boundaries. **e.** Illustration of the maximum possible increase of the subunit orientation θ upon one turn around the loop of panel **d.** **f.** Example of maximum possible decrease of the subunit orientation θ upon one turn around the loop of panel **d.** **g.** Construction of the grain boundary geometry surrounding a topological defect with winding number -1 . *Inset:* local structure of the inner boundary of the -1 defect. We observe that the tangential vector of every fourth edge of the orange boundary is orthogonal to the subunit orientation, while the others make an angle $\pm\pi/6$ with it. **h.** Examples of assemblies with many topological defects. We recall that a contour that encloses several defects has a winding number equal to the sum of the winding numbers of the individual defects [10]. From left to right: convex assembly with winding number $+1$ (the outer boundary encloses five $+1$ defects and four -1 defects), assembly whose outer boundary is associated with a large positive winding number (the outer boundary encloses five $+1$ defects and no -1 defects), and assembly with a large negative winding number (the outer boundary encloses no $+1$ defects and four -1 defects).

where the second equality again uses Stokes' theorem. In Eq. (55), the line integral runs along the outer perimeter of the whole assembly in the counterclockwise direction, and in the clockwise direction along the surface of any internal holes.

The perimeter of our assembly is comprised of a collection of subunit edges, and the value of the tangent vector $\hat{\mathbf{t}}$ thus always matches the discrete orientations of these edges. Let us consider an individual subunit, *e.g.*, in Fig. S8b. It is clear that relative to the orientation vector $\hat{\mathbf{s}}$ of this subunit, the orientation of the edge vector $\hat{\mathbf{t}}$ can only be

$\pm\pi/6$, $\pm\pi/2$ or $\pm5\pi/6$. We thus always have $\hat{\mathbf{s}} \cdot \hat{\mathbf{t}} \leq (\hat{\mathbf{s}} \cdot \hat{\mathbf{t}})_{\max} = \sqrt{3}/2$. Using Eq. (55), this implies

$$0 \leq N_d \leq \frac{2}{\sqrt{3}a} \oint_{\partial\Omega} (\hat{\mathbf{s}} \cdot \hat{\mathbf{t}})_{\max} d\ell = P. \quad (56)$$

Here P is the perimeter of the assembly counted in units of the subunit edge length. This perimeter includes the length of the surface of any internal holes. In an assembly where this upper bound would be reached, the defect energy would play the same role as a negative surface tension (assuming $\epsilon_d < \epsilon_c$).

In the system considered in Figs. 2 and 3 of the main text, the case that comes closest to the upper bound of Eq. (56) is that of the ideal vortex assembly. There the dot product $\hat{\mathbf{s}} \cdot \hat{\mathbf{t}}$ is maximized at every site of the outer perimeter of the assembly, but not in the internal hole, resulting in

$$N_d = P - 12. \quad (57)$$

This offset between the actual maximal value of N_d and the upper bound of Eq. (56) results from the microscopic details of our model, and turns out to be crucial in allowing self-limiting assembly. This can be seen in the example of the invalid design of Fig. 4i of the main text. There, the maximum number of defect interfaces is exactly equal to $P/2$, and therefore proportional to P . The defect energy thus acts exactly as a correction to the assembly surface tension. As a result, the only transition in the assembly ground state morphology is between an absence of growth (for a positive effective surface tension) to unbounded growth (for a negative effective surface tension).

Equation (56) implies a severe restriction on the number of defect interactions allowed in a large assembly. In an infinite bulk without an extensive number of holes this result imposes a vanishingly small fraction of defect interactions, as stated in the main text. In addition, in assemblies characterized by a single length scale such as the one of Fig. 1a of the main text, the number of defect interactions must at most scale like the lateral size of the assembly rather than its area. This statement forms the basis of the scaling reasoning presented in the caption of Fig. 1a of the main text.

4 Topological and Energetic Constraints Resulting from the Interaction Rules

As implied by its name, a vortex assembly is centered around a single topological defect with winding number +1. One might speculate that the vectorial nature of our order parameter could allow for defects with any other integer winding number. However we do not observe them in simulations, nor do we reproducibly observe single assemblies including more than one vortex. Here we discuss the geometrical and energetic constraints that account for these observations. This additionally allows us to rationalize why our assemblies never take the form of a bulk with an extensive number of holes.

Convex Real-space Loops Can Have Winding Numbers -1, 0 or 1

We first demonstrate a geometrical limitation imposed by our choice of interactions between subunits. For simplicity we present a coarse-grained argument where the defective grain boundaries between domains with different orientations θ are straight lines instead of straight-on-average zigzagging lines. As illustrated in Fig. S8c, in that setting the orientations θ of the subunits on either side of the boundary make angles $\pm\pi/6$ with the normal to the boundary, or $\pm5\pi/6$ depending on the conventional choice of the direction of this normal.

We consider a differentiable closed loop fully comprised within our assembly (Fig. S8d). We parametrize it by its curvilinear coordinate $u \in [0, \ell]$ where ℓ is the total length of the loop. We choose u in such a way that it increases when traveling along the loop in the counterclockwise direction, and denote the angle of its tangent vector $\hat{\mathbf{t}}(u)$ with the horizontal axis by $\phi(u)$. We consider a convex curve with a turning number of one, *i.e.*, one whose tangent has a winding number of one (qualitatively, a closed curve that loops only once). This implies

$$\forall u \in [0, \ell] \quad \frac{d\phi}{du}(u) \geq 0 \quad \text{and} \quad \phi(u) \in [0, 2\pi]. \quad (58)$$

We denote by $\theta(u)$ the map that gives the subunit orientation of a point with curvilinear coordinate u .

Close to a grain boundary our closed loop is locally a straight line, which we represent by a dashed line in Fig. S8c. Thus any point where the loop intersects the boundary realizes either one of the following scenarios corresponding to the two panels of Fig. S8c:

- **Case 1:** The tangent to the loop is about to poke through the boundary in the same direction as the orientation vectors $\hat{\mathbf{s}}$, which is equivalent to stating that $-\frac{\pi}{3} < \phi - \theta < \frac{2\pi}{3}$. Then $\theta(u)$ increases by an amount $\pi/3$ as the loop crosses the boundary.

- **Case 2:** The tangent to the loop is about to poke through the boundary in the opposite direction compared to the orientation vectors $\hat{\mathbf{s}}$, which is equivalent to stating that $\frac{2\pi}{3} < \phi - \theta < \frac{5\pi}{3}$. Then $\theta(u)$ decreases by an amount $\pi/3$ as the loop crosses the boundary.

This implies that the angle θ cannot increase if $\frac{2\pi}{3} \leq \phi - \theta \leq \frac{5\pi}{3}$, and that it cannot decrease if $-\frac{\pi}{3} \leq \phi - \theta \leq \frac{2\pi}{3}$. As shown in Fig. S8e-f, these conditions divide the (ϕ, θ) plane in three types of regions: those where only an increase of θ by increments of $\pi/3$ is possible; those where only a decrease of θ by decrements of $\pi/3$ is possible; and the boundaries between those two types of regions, where the loop runs parallel to the grain boundary and θ can neither increase nor decrease.

We point out two trajectories on these schematics. Since ϕ is an increasing function of u , we parametrize the trajectory along our convex loop by ϕ instead of u :

- Figure S8e shows a trajectory of maximum possible increase of θ . We start with $\theta \in (-\pi/3, 0)$, which places us in a region where increases are allowed. We immediately increase θ by three increments of $\pi/3$. The trajectory is then stuck in a no-increase region. We must then wait for ϕ to increase to again find ourselves in the region that allows θ to increase. When that happens, we increase θ by $\pi/3$. We renew the operation whenever possible until ϕ reaches 2π . Clearly this trajectory is constrained to lie strictly below the $\theta = \phi + \pi$ green dashed line. Thus its end point $\theta(\ell)$ lies strictly below the end point of the dashed line, whose vertical coordinate is 3π , *i.e.*, $\theta(\ell) < 3\pi$. Recalling our assumption that $\theta(0) > -\pi/3$, this implies $\theta(\ell) - \theta(0) < 10\pi/3$. In other words, the total increase of θ over the trajectory is bounded by above by $10\pi/3$.
- Figure S8f shows a trajectory of maximum possible decrease of θ . We start with $\theta \in (4\pi/3, 5\pi/3)$, which immediately allows for three consecutive decreases by $\pi/3$ each. The trajectory is then stuck in a no-decrease region, and must wait until ϕ increases by a little less than π to undergo three additional consecutive decreases. This scenario then repeats itself once. The whole trajectory must remain above the $\theta = \phi - 11\pi/3$ red dashed line. A similar reasoning to the one detailed above in our discussed of Figure S8e thus implies that the total decrease of θ over the course of the trajectory is bounded by below by $-10\pi/3$.

This reasoning thus implies

$$-\frac{10\pi}{3} < \theta(\ell) - \theta(0) < \frac{10\pi}{3}. \quad (59)$$

Since the continuity of the orientation field additionally imposes that $\theta(\ell) = \theta(0) \pmod{2\pi}$, we conclude θ can only change by -2π , 0 or 2π . The geometry of our defect interactions thus only allows winding numbers of the order parameter over our convex closed loop with values -1 , 0 or $+1$.

Isolated Point-like Defects Can Only Have Winding Number +1

Consider a large assembly with one or more isolated topological defects, which we take to mean that we can individually enclose each of them in a finite-size convex loop as in Fig. S8d. As a result of the property proved above, the winding number associated with such an isolated defect is either $+1$ or -1 . Here we show that the geometry of our interactions forces the -1 defects to have a finite core size (*i.e.*, prevents them from being point-like), which compromises its local stability.

We recall that the winding number of a defect is defined by considering the change in the angle $\theta(u)$ as u goes around a loop that encloses it. In the case of a counterclockwise loop, a $+1$ defect is characterized by a 2π -increase of θ , *i.e.*, the vector $\hat{\mathbf{s}}$ undergoes one counterclockwise rotation as we go around the loop. Conversely, a -1 defect corresponds to a decrease by -2π or equivalently a clockwise rotation of $\hat{\mathbf{s}}$. A -1 defect must thus be surrounded by crystalline domains with all six possible subunit orientations in the opposite order to that of the orientations found around a vortex assembly, which we illustrate in Fig. S8g. As shown there, the relative orientations of these domains fixes the orientation of the grain boundaries between them according to our interaction rules. This construction makes it evident that lines cannot be extended indefinitely without intersecting their counterparts. Since our interaction rules forbid an interface between two domains whose orientations differ by $2\pi/3$, these intersections must either give rise to a defect or occur at the outer boundary of the assembly. As shown on the right of Fig. S8g, the orientation of the grain boundaries imposes that the horizontal size of the -1 defect is of the order of the vertical distance between these two defects or outer boundaries; therefore isolated -1 defects are not point-like.

To assess the cost of opening such a defect, we note in the inset of Fig. S8g that a quarter of the edges that constitutes its inner boundary has $\hat{\mathbf{t}} \cdot \hat{\mathbf{s}} = 0$ while the other three quarters have $\hat{\mathbf{t}} \cdot \hat{\mathbf{s}} = \sqrt{3}/2$. Equation (55) thus implies that the total energy per unit length associated with the defect's inner boundary is $3/4(\epsilon_d - \epsilon_c) - \epsilon_c/2 = 3/4\epsilon_d - 5/4\epsilon_c$.

In cases where this energy is negative, *i.e.*, whenever $\epsilon_c > 3\epsilon_d/5$, such defects tend to gain energy by extending laterally. As demonstrated in Sec. S31, this condition is fulfilled in all regimes of the phase diagram of Fig. 2b of the main text where finite vortices form. As a result, an extended isolated -1 defect that forms at the center of a large assembly locally tends to grow until it spans across the whole assembly and splits it in half, thereby deleting itself.

Convex Assemblies with a Single Vortex are Favored Over Other Defective Assemblies

Beyond assemblies containing a single isolated topological defect, we now discuss assemblies with multiple defects. This discussion provides some assembly-wide insights on their stability which complement the local arguments discussed in the previous paragraph. For the purpose of this discussion we distinguish between convex and non-convex assemblies, *i.e.*, between assemblies whose outer boundary (colored orange in Fig. S8) is a convex curve and those for which it is not.

We first consider a convex assembly and draw a loop along its outer boundary. Our previous result implies that the net winding number of all defects contained within this loop is -1 , 0 or $+1$. They thus contain as many $+1$ defects as -1 defects plus or minus one unit. We illustrate one such assembly in Fig. S8h. Let us discuss its defect energy as well as its surface energy while approximating the $+1$ topological defects as point-like, implying that their contribution to the line integral of Eq. (55) is negligible. The finite-size -1 defects, which cannot be point-like as previously discussed, contribute to this integral to the rate of $3/4$ per unit length. To leading order in the assembly perimeter P , the number of defects in the assembly is thus

$$N_d = \left[(1-f) + \frac{3}{4}f \right] P + \mathcal{O}(P^0) = \left(1 - \frac{f}{4} \right) P + \mathcal{O}(P^0), \quad (60)$$

where $f \in (0, 1)$ is the fraction of the total assembly perimeter associated with an inner boundary. By contrast, breaking up the same number of subunits into a set of vortex assemblies with the same perimeter would result in a larger number of defects $N_d = P + \mathcal{O}(P^0)$ [see Eq. (57)]. The latter option has the same surface energy as the large, multiple-defect assembly, but a more favorable defect energy, and is thus the energetically preferred outcome.

As illustrated in Fig. S8h, non-convex assemblies may display arbitrary large positive or negative winding numbers. Both types of assemblies display the same types of inner boundary which contribute to the integral of Eq. (55) at an average rate of $3/4$, plus additional boundaries which are perpendicular to the subunit orientations and thus do not contribute at all. The basic energetic argument made above for a convex assembly therefore equally applies here, and is compounded by an additional surface energy cost due to the creation of new assembly boundaries that run perpendicular to the local subunit orientation.

Overall, these arguments indicate that multiple-defect assemblies are less energetically favorable than vortex assemblies. This rationalize the absence of multiple-defect as well as non-convex assemblies in the results presented in the main text.

S6 Supplementary Figures

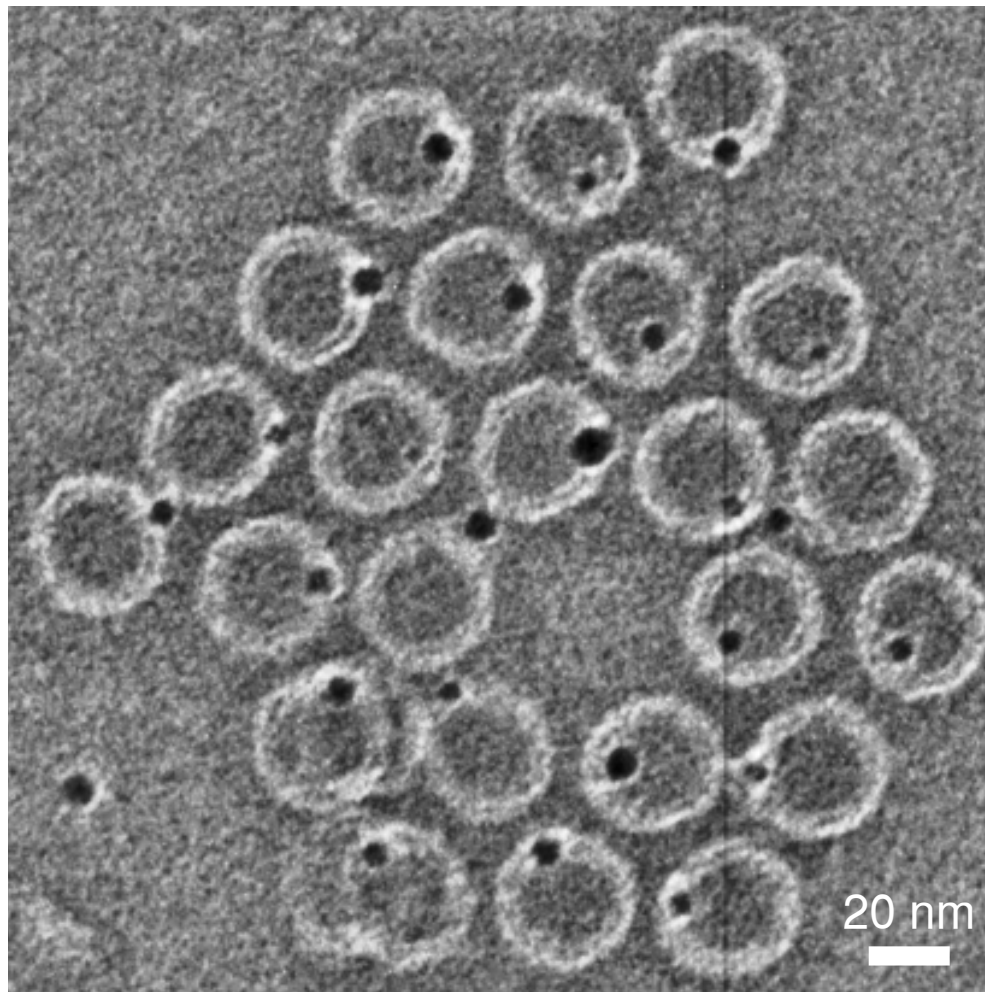


Figure S9. **TEM micrograph of an AuNP labeled vortex assembly.** This micrograph shows the same assembly as Fig. 3d with annotations removed for visibility. Here $\epsilon_c/\epsilon_d = 0.5$.

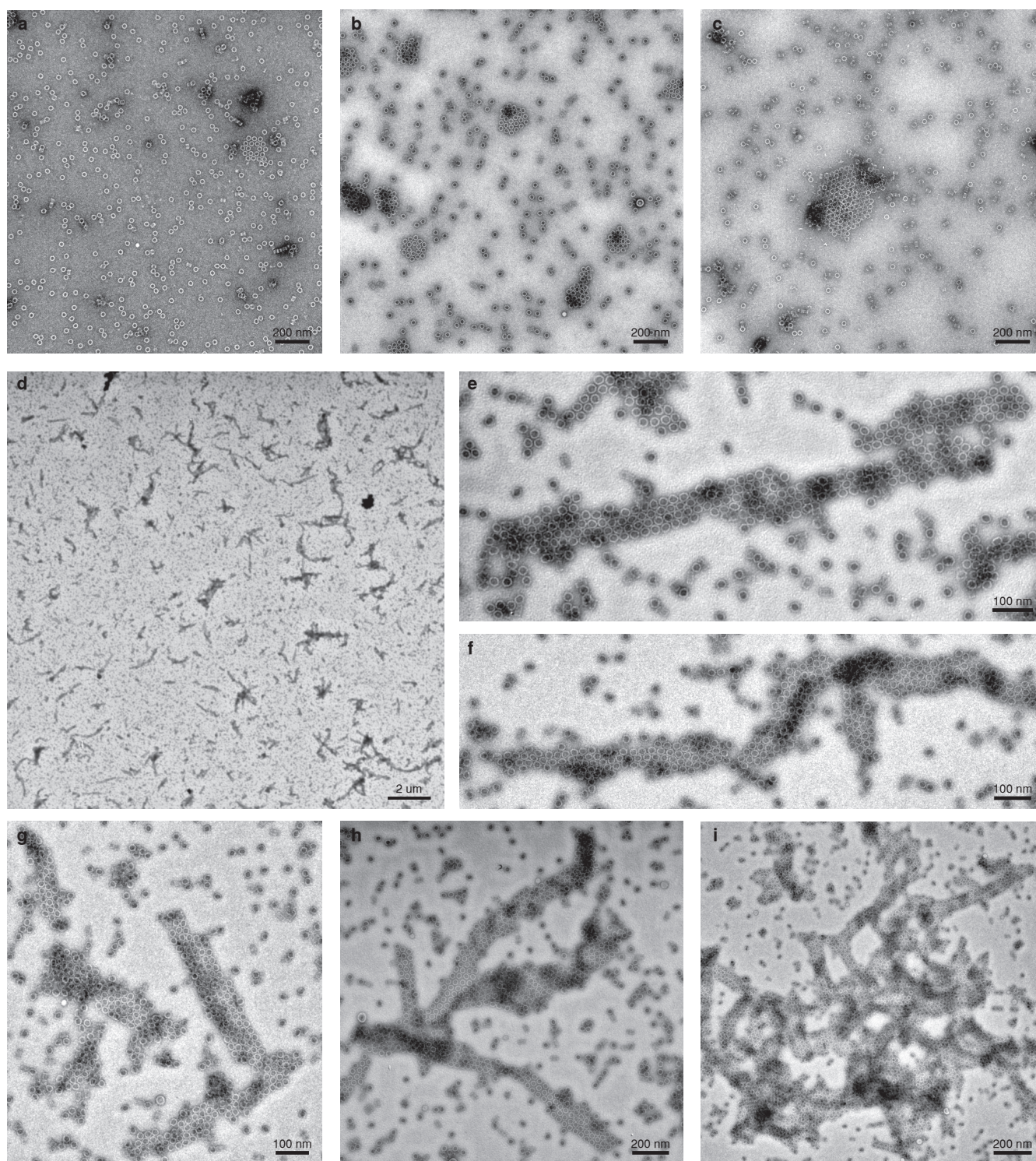


Figure S10. **TEM micrographs of self-limited vortex and fiber assemblies with DNA origami.** **a.** Typical field of view of vortex assemblies at $\epsilon_c/\epsilon_d = 0.33$. **b.** Typical field of view of vortex assemblies at $\epsilon_c/\epsilon_d = 0.5$. **c.** Typical field of view of vortex assemblies at $\epsilon_c/\epsilon_d = 0.6$. **d.** Typical field of view of fiber assemblies at $\epsilon_c/\epsilon_d = 0.5$. **e-f.** Close-ups on standalone fibers under the same conditions. **g-i.** Close-ups on overlapping and branching fibers under the same conditions.

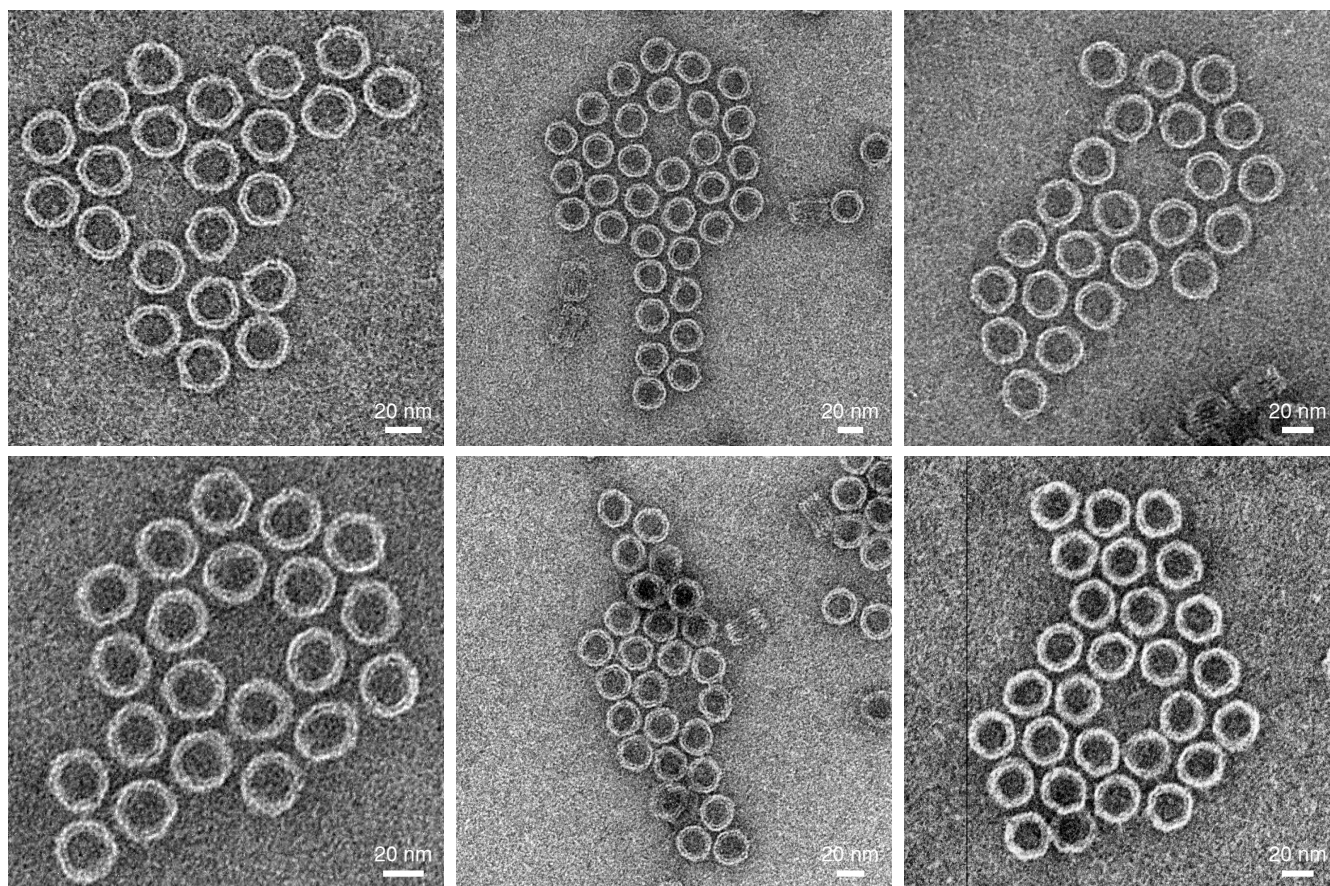


Figure S11. **TEM micrographs of vortex assemblies.** These images show defect-interaction-induced appendages reminiscent of those observed in the numerical simulation of Fig. 2c of the main text. Another instance of these appendages is visible on the micrograph of Fig. 3c of the main text.

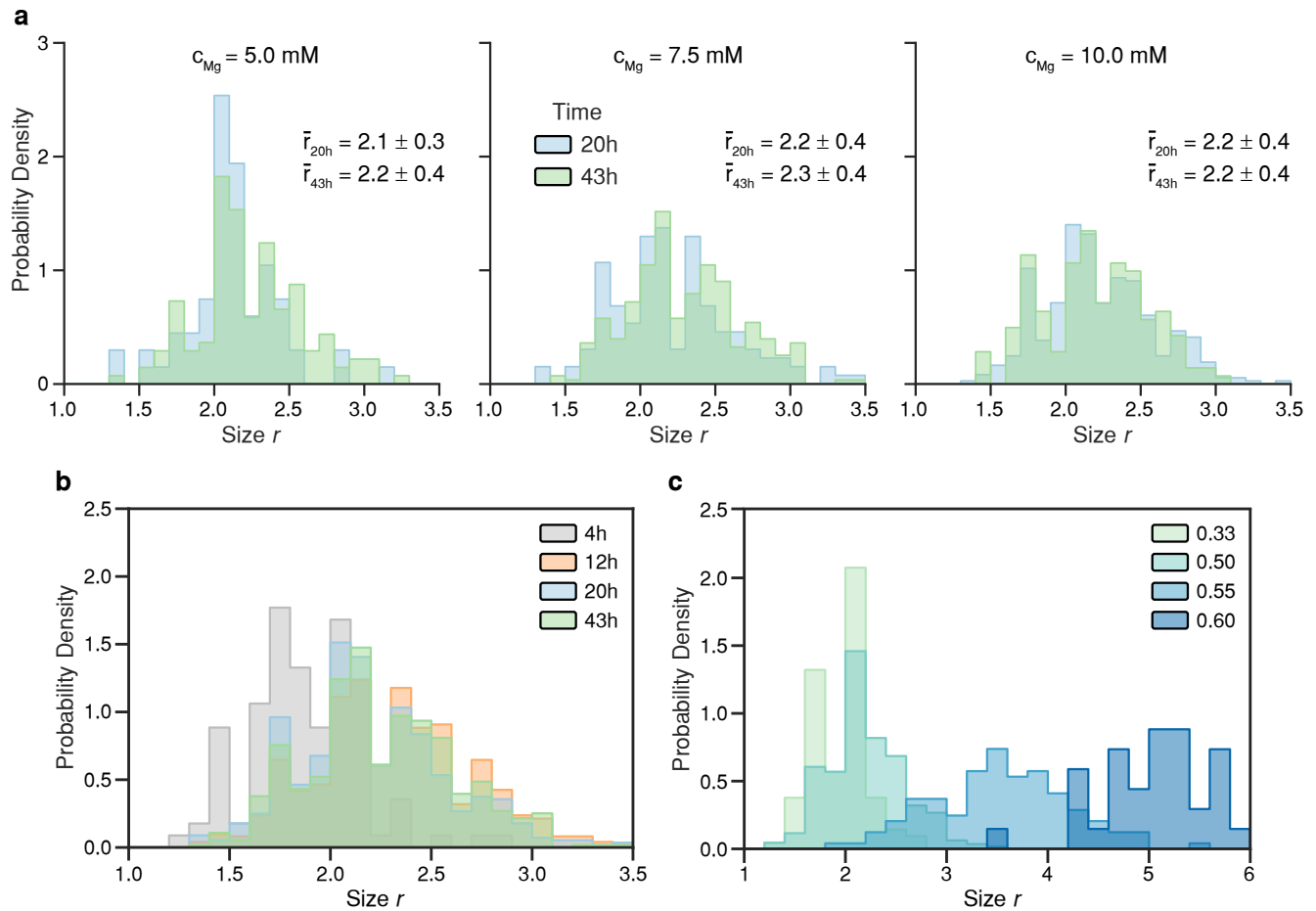
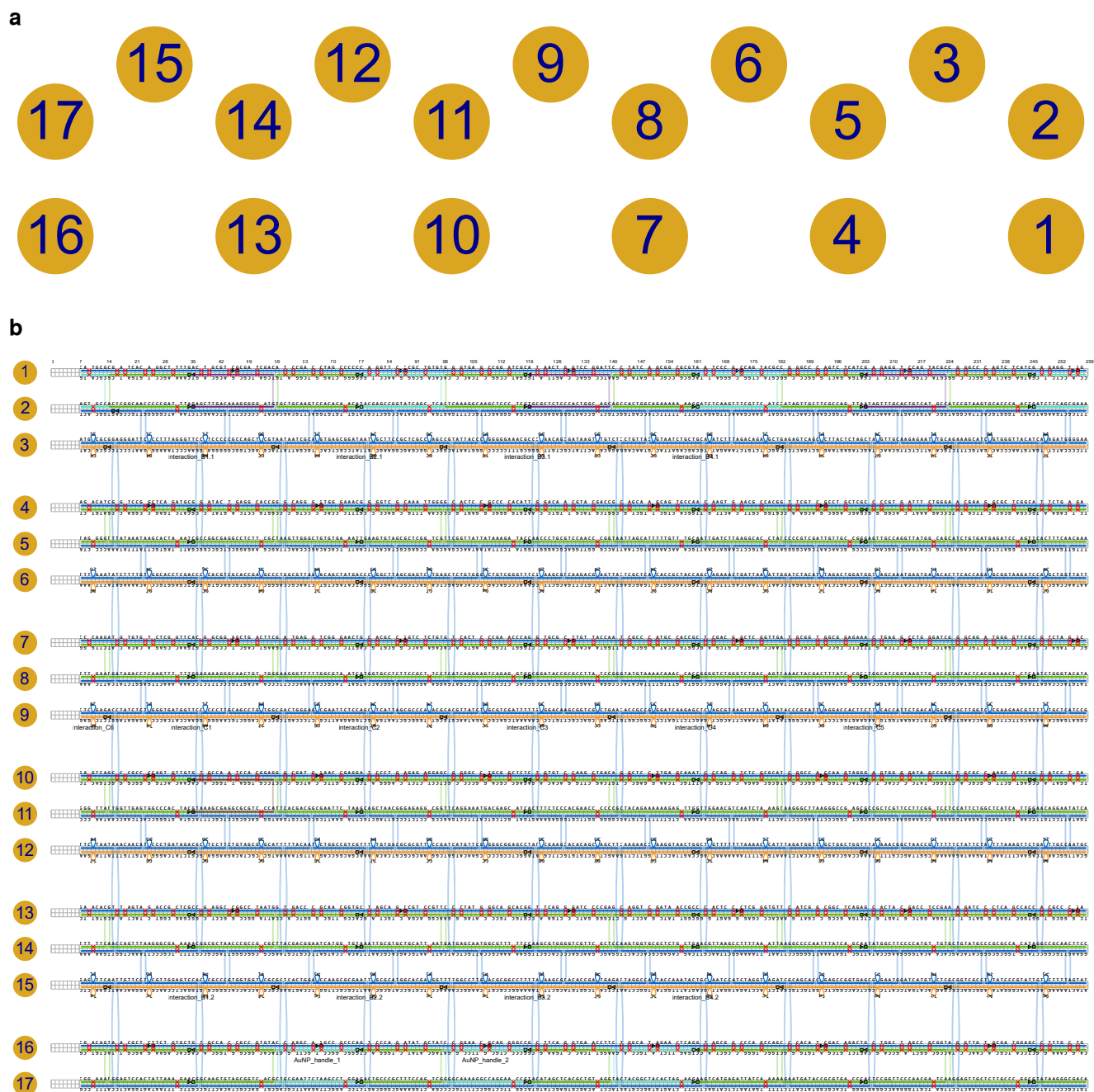


Figure S12. **Full histograms of experimental assembly sizes for the data shown in Figs. 3e-h of the main text.** **a.** Size distributions for isothermally self-assembled samples ($\epsilon_c/\epsilon_d = 0.5$) for 20 h and 43 h respectively. MgCl_2 concentrations of 5 mM ($N_{20\text{h}} = 67$, $N_{43\text{h}} = 137$), 7.5 mM ($N_{20\text{h}} = 131$, $N_{43\text{h}} = 278$) and 10 mM ($N_{20\text{h}} = 364$, $N_{43\text{h}} = 141$) were screened. Errors of mean radii represent Bessel corrected sample standard deviations. **b.** Time series of size distribution of isothermally self-assembled samples ($\epsilon_c/\epsilon_d = 0.5$, $[\text{MgCl}_2] = 5 \text{ mM}$, $N_{4\text{h}} = 113$, $N_{12\text{h}} = 1223$, $N_{20\text{h}} = 562$, $N_{43\text{h}} = 556$). A Kolmogorov–Smirnov p-value test reveals the similarity between histograms at different timepoints with $p_{12\text{h} \rightarrow 20\text{h}} = 0.12$ and $p_{20\text{h} \rightarrow 43\text{h}} = 0.07$, indicating the convergence of the underlying distribution towards a steady state. **c.** Size distributions for isothermally self-assembled samples ($t = 20 \text{ h}$, $[\text{MgCl}_2] = 5 \text{ mM}$) for $\epsilon_c/\epsilon_d = 0.33, 0.5, 0.55$ and 0.6 respectively. ($N_{0.33} = 106$, $N_{0.5} = 562$, $N_{0.55} = 122$, $N_{0.6} = 39$).



S7 Supplementary Tables

DNA Origami p2873 Scaffold Strand Sequence

p2873 scaffold sequence
GTGGCACTTTTTCGGGGAAATGTGCGCGGAACCCCTATTTGTTTATTTTCTAAATACATTCAAATA TGTATCCGCTCATGAGACAATAACCCTGATAAATGCTTCAATAATATTGAAAAAGGAAGAGTATGA GTATTCAACATTTCCGTGTCGCCCTTATTCCTTTTTTTCGCGCATTTTGCCTTCCTGTTTTTGCTC ACCCAGAAACGCTGGTAAAAGTAAAAGATGCTGAAGATCAGTTGGGTGCACGAGTGGGTACATCG AACTGGATCTCAACAGCGGTAAGATCCTTGAGAGTTTTTCGCCCGAAGAAGCTTTTCCAATGATGA GCACTTTTAAAGTTCTGCTATGTGGCGCGGTATTATCCCGTATTGACGCCGGGCAAGAGCAACTCG GTCGCCGCATACACTATTCTCAGAATGACTTGGTTGAGTACTCACCAGTCACAGAAAAGCATCTTA CGGATGGCATGACAGTAAGAGAATTATGCAGTGTGCCATAACCATGAGTGATAAACTGCGGCCA ACTTACTTCTGACAACGATCGGAGGACCGAAGGAGCTAACCGCTTTTTTGCACAACATGGGGGATC ATGTAAGTTCGCCTTGATCGTTGGGAACCGGAGCTGAATGAAGCCATACCAAACGACGAGCGTGACA CCACGATGCCTGTAGCAATGGCAACAACGTTGCGCAAACTATTAAGTGGCGAACTACTTACTCTAG CTTCCCGGCAACAATTAATAGACTGGATGGAGGCGGATAAAGTTGCAGGACCACTTCTGCGCTCGG CCCTTCGGGCTGGCTGGTTTATTGCTGATAAATCTGGAGCCGGTGAGCGTGGGTACGCGGTATCA TTGCAGCACTGGGGCCAGATGGTAAGCCCTCCCGTATCGTAGTTATCTACACGACGGGGAGTCAGG CAACTATGGATGAACGAAATAGACAGATCGCTGAGATAGGTGCCTCACTGATTAAGCATTTGGTAAC TGTGACACCAAGTTTACTCATATATACTTTAGATTGATTTAAAACCTCATTTTTAATTTAAAAGGA CTAGAGTGAAGATCTTTTTGATAATCTCATGACCAAATCCCTTAACGTGAGTTTTCGTTCCGAT GAGCGTCAGACCCCGTAGAAAAGATCAAAGGATCTTCTTGAGATCCTTTTTTTCTGCGCGTAATCT GCTGCTTGCAAACAAAAAACCACCGCTACCAGCGGTGGTTTGTGTTGCGCGATCAAGAGCTACCAA CTCTTTTTCCGAAGGTAAGTGGCTTCAGCAGAGCGCAGATACCAAATACTGTTCTTCTAGTGTAGC CGTAGTTAGGCCACCACTTCAAGAACTCTGTAGCACCGCCTACATACCTCGCTCTGCTAATCCTGT TACCAGTGGCTGCTGCCAGTGGCGATAAGTCGTGTCTTACCGGGTTGACTCAAGACGATAGTTAC CGGATAAGGCGCAGCGGTTCGGGCTGAACGGGGGGTTTCGTGCACACAGCCCAGCTTGGAGCGAACGA CCTACACCGAAGTGAATACCTACAGCGTGAGCTATGAGAAAGCGCCACGCTTCCCAGGGGAGAA AGCGGACAGGTATCCGGTAAGCGGCAGGTCGGAACAGGAGAGCGCACGAGGGAGCTTCCAGGGG GAAACGCCTGGTATCTTTATAGTCTCTGTCGGGTTTCGCCACCTCTGACTTGAGCGTCGATTTTTGT GATGCTCGTCAGGGGGGCGGAGCCTATGAAAAACGCCAGCAACGCGGCCTTTTTACGGTTTCTG CCTTTTTGCTGGCCTTTTGTCTACATGTTCTTTCCTGCGTTATCCCCTGATTCTGTGGATAACCGTA TTACCGCCTTTGAGTGAGCTGATACCGCTCGCCGACGCCAAGACCGAGCGCAGCGAGTCAGTGA GCGAGGAAGCGGAAGAGCGCCCAATACGCAAACCGCCTCTCCCCGCGCGTTGGCCGATTCATTAAT GCAGCTGGCAGCAGAGTTTCCCAGCTGGAAAGCGGGCAGTGAGCGCAACGCAATTAATGTGAGTT AGCTCACTCATTAGGCACCCAGGCTTTACACTTTATGCTTCCGGCTCGTATGTTGTGTGGAATTG TGAGCGGATAACAATTTACACAGGAAACAGCTATGACCATGATTACGCCAAGCGCAATTCTCCA GGCTTAGAATTCGCTCACTGGCCGTCGTTTTACACCATGATTACGCCAAGCGCGAATTCTCCAGGC TTAGAATTCGCTCACTGGCCGTCGTTTTACAACGTCGTGACTGGGAAAACCCCTGGCGTTACCCAAC TTAATCGCCTTGCAGCACATCCCCCTTTCGCCAGCTGGCGTAATAGCGAAGAGGCCCGCACCGATC GCCCTTCCCAACAGTTGCGCAGCCTGAATGGCGAATGGGACGCGCCCTGTAGCGGCGCATTAAAGCG CGGCGGGTGTGGTGGTTACGCGCAGCGTGACCGCTACACTTGCCAGCGCCCTAGCGCCCCGCTCCTT TCGCTTTCTTCCCTTCCCTTCTCGCCACGTTTCGCCGGCTTTCCCGTCAAGCTCTAAATCGGGGGC TCCCTTTAGGGTTCGATTTAGTGCTTTACGGCACCTCGACCCCAAAAACTTGATTAGGGTGATG GTTACGTTAGTGGGCCATCGCCCTGATAGACGGTTTTTTCGCCCTTTGACGTTGGAGTCCACGTTCT TTAATAGTGGACTCTTGTTCCAAACCTGGAACAACACTCAACCCTATCTCGGTCTATTCTTTTGATT TATAAGGGATTTGCGGATTTTCGGCCTATTGGTTAAAAAATGAGCTGATTTAACAAAAATTTAACG GAATTTTAACAAAATATTAACGCTTACAATTTAG

Table S3: DNA sequence of scaffold strand p2873

DNA Origami Base Staple Sequences

Identifier	Sequence
SCAF1[130]1[171]	GTCCGGATTCCCTATCAGCGGCGCGTAATCCCC
SCAF1[172]1[213]	CCAGTACGCCGGGCCAGTCTCATCGAGAGGT
SCAF1[214]1[255]	CCAGTACGCCGGGCCAGTCTCATCGAGAGGT
SCAF1[256]1[45]	GGCATGCGCGATCACAGGCTTTTACTGCGTC
SCAF1[46]1[87]	GCGATCGACATCCGACCTAGCCCCCAGGTTC
SCAF1[88]1[129]	CCGCTGTGTGGGTGAGCCGGATCGCATAACTG
SCAF4[109]4[150]	GCCCCACATTGGACAACGTACGACCGCAGCAA
SCAF4[151]4[192]	GCAGTGCCAACAAGTGAACGCCACGGTTCGTC
SCAF4[193]4[234]	GCCTGCTCGCCCCGTGATTTCTGGGAACGAAG
SCAF4[235]4[24]	GCGCTCGGCATTCTGAGAAGACATCGGTCCGG
SCAF4[25]4[66]	CTCAGATGCGGATACTGAGGCACCGGGCAGGG
SCAF4[67]4[108]	GTGGGAAACGGGGTCGCAAAATGGGGCACTCC
SCAF7[130]7[171]	TTGTTACCAATCGCCCATGCCACCGCTCGACG
SCAF7[172]7[213]	GCTCGGTTGATGCGGTGGCGGAGAAAAGTGGG
SCAF7[214]7[255]	CCTGGGATCGGGCAGATGGGGTTTCGCGTCTAG
SCAF7[256]7[45]	GCCCCAAGATGTGTGTCTCGGTTACGCGCGGA
SCAF7[46]7[87]	GCTGACTTCGATGAGGTGCGGAACTGCACGCC
SCAF7[88]7[129]	GGTCTCTGTGTCACTCCCGAACCAGGTGCGC
SCAF10[109]10[150]	TGCGGCTCTCTGTGTCCAAGCTGACAGGCTCC
SCAF10[151]10[192]	TTGAGCAAATCCCAGGTCTCGCGCATCGGCCA
SCAF10[193]10[234]	CCAAGTAGGGAGTGGGGATAGCCGAGTGCGCC
SCAF10[235]10[24]	AAGCACTCGGTATCCTGAGAGTCAGCCCCGCC
SCAF10[25]10[66]	CAGTGTGTGTGCCAATCCACGGAGGGCGATG
SCAF10[67]10[108]	GAACCGAGGATCCCTGAGAGAGGAGCGGGGCC
SCAF13[130]13[171]	GATCCCCGAGCAGGTGCGATAACCGCCCCTCC
SCAF13[172]13[213]	CTCGGGTGTTCATCGGCGGCTCAGAGCACTAC
SCAF13[214]13[255]	GACCTCCGAAAGATCCCTCAGCCACCACGCC
SCAF13[256]13[45]	GAGAACACGTTAGTAGACCGCTCGCCGAGGCC
SCAF13[46]13[87]	GGCCTAATGGTGACCCGCAACGGTGCTAGCAG
SCAF13[88]13[129]	TCGTCCGTTCCCTATGGGCAGCACGGTTCAGG
SCAF16[109]16[150]	GCAGGGGCCGCTTCAGGTGAACCTTCTGGCAT
SCAF16[151]16[192]	AGAACTCAGGTAGCGGCCAGCCAGCCCACAT
SCAF16[193]186[234]	CGACAGACTGCTGGCTAGCCGCGGTAGGTTGT
SCAF16[235]16[24]	GCGATGGAGCCCTTTGCTGCGACAGTAACGCTC
SCAF16[25]16[66]	TTCTGTGCTGTGCCACCGCGGTACCAAGCA
SCAF16[67]16[108]	GCCGCCCAGTCCCAGATATGCTATCCGGAAC
ST1[118]2[118]	CGATCCGGCTCACCCACTCAAAGGCAAGCTCCCTCG
ST1[160]2[160]	CGCGCCGCTGATAGGAAGCCACTGGCAGAAAAAAG
ST1[202]2[202]	ATGAGACTGGGCCCGGCATAGTTGCTTCGCCAGTTA
ST1[244]2[244]	ATGAGACTGGGCCCGGATCCGTAAGTGCACCCAACT
ST1[34]2[34]	CAAAAGCCTGTGATCGACTCGGCAACCCCCGATTTA
ST1[76]2[76]	GGGGCTAGGTCGGATGTGCTGCAAGTCCACACAACA
ST2[119]1[119]	TGCGCTCTCCCACTGGCAGCATCCGGACCAGTTATG
ST2[161]1[161]	GATCTCAAGTTTCGTTTCATCCGTAAGTGGCGGGATTA
ST2[203]1[203]	ATAGTTTGCACTGTCCATGCCGTAAGTGGACCTCTCG
ST2[245]1[245]	GATCTTCAGCGAAAAGTGGCCCGCATGCCACCTCTCG
ST2[35]1[35]	GAGCTTGACAAAGGGGATGTCGATCGCGACGCAGT
ST2[77]1[77]	TACGAGCCGGTATCAGCTCACACAGCGGGAACCTGG
ST3[13]3[224]	GCGCACATTTCCCCATCTTTTGTGTAACCCACTCGATGCTTTCT
ST3[223]3[182]	GCATAATTCTCTTGCAACGTTAGCTAGAGTAAGTAGCTGACTCTC
ST4[118]5[118]	TGTGGGGCGGAGTGCCTTCGGTTATTATAAAGATAC
ST4[160]5[160]	GGCACTGCTTGCTGCGTAATTAGCATTTTTGTTTGC
ST4[202]5[202]	GAGCAGGCGACGAACCTCCCCGTCGATTGTTGCCGG
ST4[244]5[244]	CCGAGCGCCTTCGTTCCATCTGTGATGAGATCCAGT
ST4[34]5[34]	CATCTGAGCCGGACCGTTTATAAATAAGCACTAAAT
ST4[76]5[76]	TTCCCACCCCTGCCCTAAGTTGGGCTGTGTGAAAT
ST5[119]4[119]	CAACCCTGCTCCAACCCGGGTCGTACGTTGTCCAA
ST5[161]4[161]	AATGATCTTGAGGCACCTAGTGGCGTTCCTTGT

Identifier	Sequence
ST5[203]4[203]	GAGTTGCCAGGTTATGGCAGCCAGAAATCACGGGGC
ST5[245]4[245]	TCACITTTCAACAAATAGGGGATGTCTTCTCAGAATG
ST5[35]4[35]	CGCCGGCGAGGCCTCTTCGCGGTGCCTCAGTATCCG
ST5[77]4[77]	TGAAGTGTAGCGCTCGGTCGCCAATTTGCGACCCCG
ST6[118]6[77]	AACCCGACAGGACCCACAGAGCTCACTGACTCGCTAAGCCTGGGG
ST6[160]6[119]	GGTAGCGGTGGTTGAGCGAGTAACTATCGTCTTGACGCTTACCGA
ST6[202]6[161]	ATCCAGTCTATTATGTAGATCCAATGCTTAATCAGTTTCTACGCT
ST6[244]6[203]	ATCTTACCGCTGTCTGGTGAAGTGTATCACTCATTGCTACACC
ST6[34]6[245]	TCGAGGTGCCGTACAAAAGATATTTAGAAAAATAACCAGCGTTGG
ST6[76]6[35]	TCATAGCTGTTTCTAACGCCAGGGCGATCGGTGCGACGTGGCCGGG
ST7[118]8[118]	GGTTCGGGAGTGACATCATCAGGGAGTCAGAGGTG
ST7[160]8[160]	GGTGGCATGGGCGATTGGGTATGTAAAACAAACCAC
ST7[202]8[202]	TCGCCACCCGCATCTAAACTACGACTTTATCCGC
ST7[244]8[244]	GAACCCCATCTGCCCGGCTACTCACGAAAACCTCTC
ST7[34]8[34]	GAACCGAGACACACATTGATAGACCTCAAGTTTTTTT
ST7[76]8[76]	GTTCCCGACCTCATCGGAAGGGTTTTTGGCGTAATC
ST8[119]7[119]	GCGGATACCGCGCCTTATCCGGTAACAAGCGCACCT
ST8[161]7[161]	CGGGGTCTGGGTCTGACAGTAACCGAGCCGTCGAGC
ST8[203]7[203]	CTGGCATCGGTAAGTTGGCCATCCCAGGCCTCAGTT
ST8[245]7[245]	AATCTGGGTACATATTTGAACTTGGGGCCTAGACGC
ST8[35]7[35]	GGAGAAAGGGCAACTGTTGGAAGTCAGCTCCGCCGT
ST8[77]7[77]	ATGGTGCTCTTCCGCTTCCCAGAGACCGGGCGTGCA
ST10[118]11[118]	GAGCCGACGGCCCCGCTTCCAGAAATGACGAGCATC
ST10[160]11[160]	TTGCTCAAGGAGCCTGCGCTACAGAAAAAAGAGTTG
ST10[202]11[202]	CTACTTGGTGCCGATTAAGGGCTTAAGGGCCGAGC
ST10[244]11[244]	GAGTGCTTGGCGCACTTCCATTCTGGCTCATCATTG
ST10[34]11[34]	CAACACTGGGGCGGGCTTGGTTGAGTGGCCCACTAC
ST10[76]11[76]	CTCGGTTCCATCGCCCTTACGACGGCGAATTCTAA
ST11[119]10[119]	ACTTCTCCCACGAACCCCTCAGCTTGGACACAGA
ST11[161]10[161]	GTTGGAACGTCAATCTAAAGGCGCGAGACCTGGGAT
ST11[203]10[203]	GCCGCTCGTTCCTTCCGGTCCCAGGCTATCCCCACTCC
ST11[245]10[245]	GAACAGGAATATCAGGGTTATGACTCTCAGGATAACC
ST11[35]10[35]	GTAAAGCGAGGCGGCTCCCATCCGTGGATTGGCACA
ST11[77]10[77]	CGACTAACGGGAGAGGCGGCTCTCTCAGGGATC
ST12[118]12[77]	GGCTCCGCCCCCGAACATGATCGGCCAACGCGCGTCACATTA
ST12[160]12[119]	CAGTTACCTTCGGGTTCTTGAAGCTGGGCTGTGTGCTTCGGGATA
ST12[202]12[161]	ACCAGCCAGCCGACCATCTAAATGAAGTTTTAAAAAACTCAGC
ST12[244]12[203]	GAACTTTAAAAGTAGAATAGAAAAAGCGGTTAGCCGTTTTGGTAA
ST12[34]12[245]	TCTATCAGGGCGATGTTGTTTATTATTGAAGCATTGGCAAAATCA
ST12[76]12[35]	CGACGGCCAGTGATTGTAAAAATGCGCCGCTACAGAAGGAGCGCG
ST13[118]14[118]	GTGCTGCCCATAGGGAGATGAGCAATGGCGTTTTTC
ST13[160]14[160]	CGGTTATCGACCTGCTCCAAGTGGTGCGCTCTGCTG
ST13[202]14[202]	CTGAGCCGCGGATGAAAAGGCCCAATTTATCAGCA
ST13[244]14[244]	TGGCTGAGGGATCTTTGCTGTATGCCCGCGCCACAT
ST13[34]14[34]	CGAGCGGTCTACTAACACAGTTTAAAGGGCGAAAA
ST13[76]14[76]	ACCGTTGCGGGTACCTTACGACGGAATCATGGTGT
ST14[119]13[119]	CAAGCGTGGGGTTCGTTTCGCTCGGGGATCCCTGAACC
ST14[161]13[161]	AACGTTAAGCCTTTTTAAATTCACCCGAGGGAGTGGG
ST14[203]13[203]	ATATGGCTTCCCATGTTGTGCGGAGGTCGTAGTGCT
ST14[245]13[245]	AGGCCGCAACTTCCTTTTTCTGTTCTCGGGCGTGG
ST14[35]13[35]	ACGGCGCTAACCCGCCGCGCATTAGGCCGGCCTCGG
ST14[77]13[77]	AAATTGCGTGCTGCATTAATACGGACGACTGCTAGC
ST15[13]15[224]	GAATACTCATACTAAAAGGGACAATACGGGATAATAGGGACCCG
ST15[223]15[182]	GAGTTACATGATCCATTCAGCGCTCACCGGCTCCAGGTGCTGCGA
ST16[160]17[160]	TGAGTTCTATGCCAGATACTACGGCTACACTAGAAG
ST16[202]17[202]	GTCTGTCTATGTGGGCGAATGATACCCGCGTGACCC
ST16[244]17[244]	TCCATCGCACAACTAAGGAGTTGCTCTTGCCCCGC
ST16[34]17[34]	GCACAGAAGAGCGTTATGGAGTCCACTATTAAAGAA
ST17[119]16[119]	TACATAGCTCACGCTGTAGGAGTTTACCTGAAGCG
ST17[161]16[161]	AAGTCATGAGATTATCAAAATGGCTGGGCCGCTACC
ST17[203]16[203]	ACTCCGGTTCCCAACGATCACCCGCGCTAGCCAGCA

Identifier	Sequence
ST17[245]16[245]	GTATAAGGGCGACACGGAAACTGTCGCAGCAAAGGC
ST17[35]16[35]	CGGCAAGTGTAGCGGTACGACACGGCGGTGGCACA
ST17[77]16[77]	GACTGCCCCGCTTCCAGTCGTAGCATATCTGGGACT
interaction_D ₁ 1	GCGTAACCACCACGGGCGCTGTGGACTCCAACGTCAGGAACAATT
interaction_D ₁ 2	ACGCCAGCTGGCGGGGAAAGGAACCCATAAAGGGAGAATCCCTCC
interaction_D ₂ 1	ACCTGTCGTGCCATGCGCTCAATTTCGCGCTTGGCGTCCAGTGAGC
interaction_D ₂ 2	GCTGCGGCGAGCGGAAGCATATTATCCGCTCACAATGCGATTATT
interaction_D ₃ 1	TCAGTTCGGTGTACGCTTCTAAAAGGCCGCGTTGCAAGGCCAAA
interaction_D ₃ 2	ACACGACTTATCGCTGTTCCGGGCGTTTCCCCCTGGGGTAATACG
interaction_D ₄ 1	TCTTCACCTAGATGGATTTTGCAGTATTTGGTATCTGGCCTAATC
interaction_D ₄ 2	AGCGATCTGTCTAAAGATCCTGCAGCAGATTACGCGTAACAGGAG
interaction_C ₁	CCATTCAGGCTGCAAGGGAAGGAACCATCACCCATAAGAGATAGGT
interaction_C ₂	CGTATTGGGCGCTAATGAGTGTCTGGAGAATTTCGCGCTCCAGTCG
interaction_C ₃	CAGCCCGACCGCTTGTCCGCCAAAAATCGACGCTCAGATAACGTG
interaction_C ₄	TATGAGTAAACTTACGCTCAGAGCTCTTGATCCGGCGGCGGTGTT
interaction_C ₅	ATCGTTGTCAGAATGGTGTCAAGAAGTGGTCCTGCAATACGGGTA
interaction_C ₆	CTCATGAGCGGATGAGCAAAAAACGTTCTTTCGGGGACCAAGTCG
AuNP_handle.1	GGGCGGCCTGCTTGGTCTGCGAATTCTAAGCCTGGA
AuNP_handle.2	GCCCCTGCGTTCGGGAGGGCAAAAGGCCAGGAACCG

Table S4: **Mini-scaffold and base staple strand sequences for a DNA origami monomer.** The prefix *interaction* is used for staple strands acting as base for single-stranded extensions used for modeling defect (D_YX) or crystalline (C_Y) interactions. Here, X describes the vertical position (top = 1 or bottom = 2) of defect linkers on a side of the DNA origami nanocylinder, whereas Y describes the side itself (see Fig. 3a of the main text).

DNA Origami Interaction Staple Sequences

Identifier	Sequence	ΔG (kcal/mol)
Interaction strands vortex $\epsilon_c/\epsilon_d = 0.33$		
interaction_D1_1_R0.33	GCGTAACCACCACGGGCGCTGTGGACTCCAACGTCAGGAACAATT TTTT AGCGCGAGCGCG	-20.94
interaction_D1_2_R0.33	ACGCCAGCTGGCGGGGAAAGGAACCCTAAAGGGAGAATCCCTCC TTTT AGCTCGCGCGCG	-20.94
interaction_D2_1_R0.33	ACCTGTCGTGCCATGCGCTCAATTCGCGCTTGGCGTCCAGTGAGC TTTT TTGCGCCGCCGC	-20.59
interaction_D2_2_R0.33	GCTGCGGCGAGCGGAAGCATATTATCCGCTCACAATGCGATTATT TTTT TTGCCCGCGCGC	-20.59
interaction_D3_1_R0.33	TCAGTTCGGTGTACGCTTTCTAAAAGGCCGCGTTGCAAGGCCAAA TTTT CGCGCTCGCGCT	-20.94
interaction_D3_2_R0.33	ACACGACTTATCGCTGTTCCGGGCGTTTCCCCCTGGGGTAATACG TTTT CGCGCGCGAGAT	-20.94
interaction_D4_1_R0.33	TCTTCACCTAGATGGATTTTGCAGTATTTGGTATCTGGCCTAATC TTTT GCGGCGGCGCAA	-20.59
interaction_D4_2_R0.33	AGCGATCTGTCTAAAGATCCTGCAGCAGATTACGCGTAACAGGAG TTTT GCGCGCGGGCAA	-20.59
interaction_C1_R0.33	CCATTCAGGCTGCAAGGGAAGGAACCATCACCTAAGAGATAGGT TTTT AAGAAAGAAGAG	-11.99
interaction_C2_R0.33	CGTATTGGGCGCTAATGAGTGTGGAGAATTCGCGCTCCCAGTCG TTTT AAAAGAGAGAG	-11.99
interaction_C3_R0.33	CAGCCCAGCGCTTGTCCGCCAAAAATCGACGCTCAGATAACGTG TTTT AAACTATAGACG	-11.92
interaction_C4_R0.33	TATGAGTAAACTTACGCTCAGAGCTCTTGATCCGGCGGCGGTGTT TTTT CTCTTCTTTCTT	-11.99
interaction_C5_R0.33	ATCGTTGTCAGAATGGTGTCAAGAAGTGGTCTGCAATACGGGTA TTTT CTCTCTCTTTTT	-11.99
interaction_C6_R0.33	CTCATGAGCGGATGAGCAAAAAACGTTCTTCGGGGACCAAGTCG TTTT CGTCTATAGTTT	-11.92
Interaction strands vortex $\epsilon_c/\epsilon_d = 0.5$		
interaction_D1_1_R0.5	GCGTAACCACCACGGGCGCTGTGGACTCCAACGTCAGGAACAATT TTTT CTATATTTAATC	-8.98
interaction_D1_2_R0.5	ACGCCAGCTGGCGGGGAAAGGAACCCTAAAGGGAGAATCCCTCC TTTT GAATTTATATAG	-8.98
interaction_D2_1_R0.5	ACCTGTCGTGCCATGCGCTCAATTCGCGCTTGGCGTCCAGTGAGC TTTT TTATATATAGTG	-9.09
interaction_D2_2_R0.5	GCTGCGGCGAGCGGAAGCATATTATCCGCTCACAATGCGATTATT TTTT TTACATATATAG	-9.09
interaction_D3_1_R0.5	TCAGTTCGGTGTACGCTTTCTAAAAGGCCGCGTTGCAAGGCCAAA TTTT GATTAAATATAG	-8.98
interaction_D3_2_R0.5	ACACGACTTATCGCTGTTCCGGGCGTTTCCCCCTGGGGTAATACG TTTT CTATATAAATTC	-8.98
interaction_D4_1_R0.5	TCTTCACCTAGATGGATTTTGCAGTATTTGGTATCTGGCCTAATC TTTT CACTATATATAA	-9.09
interaction_D4_2_R0.5	AGCGATCTGTCTAAAGATCCTGCAGCAGATTACGCGTAACAGGAG TTTT CTATATATGTAA	-9.09
interaction_C1_R0.5	CCATTCAGGCTGCAAGGGAAGGAACCATCACCTAAGAGATAGGT TTTT ATATACCTATAA	-9.42
interaction_C2_R0.5	CGTATTGGGCGCTAATGAGTGTGGAGAATTCGCGCTCCCAGTCG TTTT CAAAATTAATAT	-9.22
interaction_C3_R0.5	CAGCCCAGCGCTTGTCCGCCAAAAATCGACGCTCAGATAACGTG TTTT AAAAATAATATG	-9.22
interaction_C4_R0.5	TATGAGTAAACTTACGCTCAGAGCTCTTGATCCGGCGGCGGTGTT TTTT TTATAGGTATAT	-9.42
interaction_C5_R0.5	ATCGTTGTCAGAATGGTGTCAAGAAGTGGTCTGCAATACGGGTA TTTT ATATTAATTTTG	-9.22
interaction_C6_R0.5	CTCATGAGCGGATGAGCAAAAAACGTTCTTCGGGGACCAAGTCG TTTT CATATTAATTTT	-9.22

Identifer	Sequence	ΔG (kcal/mol)
Interaction strands vortex $\epsilon_c/\epsilon_d = 0.55$		
interaction.D ₁ 1_R0.55	GCGTAACCACCACGGGCGCTGTGGACTCCAACGTCAGGAACAATT TTTT AACAATAATATT	-9.60
interaction.D ₁ 2_R0.55	ACGCCAGCTGGCGGGGAAAGGAACCCATAAGGGAGAATCCCTCC TTTT ATATTCTACTAA	-9.71
interaction.D ₂ 1_R0.55	ACCTGTCGTGCCATGCGCTCAATTCGCGCTTGGCGTCCAGTGAGC TTTT GTCTAAATATAT	-9.36
interaction.D ₂ 2_R0.55	GCTGCGGCGAGCGGAAGCATATTATCCGCTCACAAATGCGATTATT TTTT CTFTTAATATAC	-9.24
interaction.D ₃ 1_R0.55	TCAGTTCGGTGTACGCTTTCTAAAAGGCCGCGTTGCAAGGCCAAA TTTT AAATATTATGTT	-9.60
interaction.D ₃ 2_R0.55	ACACGACTTATCGCTGTTCCGGGCGTTTCCCCCTGGGGTAATACG TTTT TTAGTAGAATAT	-9.71
interaction.D ₄ 1_R0.55	TCTTCACCTAGATGGATTTTGCAGTATTTGGTATCTGGCCTAATC TTTT ATATATTTAGAC	-9.36
interaction.D ₄ 2_R0.55	AGCGATCTGTCTAAAGATCCTGCAGCAGATTACGCGTAACAGGAG TTTT GTATATTTAAAAG	-9.24
interaction.C ₁ _R0.55	CCATTCAGGCTGCAAGGGAAGGAACCATCACCCTAAGAGATAGGT TTTT AATAAGTTCTCT	-11.69
interaction.C ₂ _R0.55	CGTATTGGGCGCTAATGAGTGCTGGAGAATTCGCGCTCCCAGTCG TTTT GATAGGATTAAG	-10.94
interaction.C ₃ _R0.55	CAGCCCCACCGCTTGTCCGCCAAAAATCGACGCTCAGATAACGTG TTTT ATFCTCATATCT	-11.48
interaction.C ₄ _R0.55	TATGAGTAAACTTACGCTCAGAGCTCTTGATCCGGCGGCGGTGTT TTTT AGAGAACTTATT	-11.69
interaction.C ₅ _R0.55	ATCGTTGTCAGAATGGTGTCAAGAAGTGGTCCTGCAATACGGGTA TTTT CTTAATCCTATC	-10.94
interaction.C ₆ _R0.55	CTCATGAGCGGATGAGCAAAAAACGTTCTTCGGGGACCAAGTCG TTTT AGATATGAGAAT	-11.48
Interaction strands vortex $\epsilon_c/\epsilon_d = 0.6$		
interaction.D ₁ 1_R0.6	GCGTAACCACCACGGGCGCTGTGGACTCCAACGTCAGGAACAATT TTTT TTAGATTATACT	-10.15
interaction.D ₁ 2_R0.6	ACGCCAGCTGGCGGGGAAAGGAACCCATAAGGGAGAATCCCTCC TTTT AGTAATTTTAAA	-10.11
interaction.D ₂ 1_R0.6	ACCTGTCGTGCCATGCGCTCAATTCGCGCTTGGCGTCCAGTGAGC TTTT ATAATATCCTAA	-9.70
interaction.D ₂ 2_R0.6	GCTGCGGCGAGCGGAAGCATATTATCCGCTCACAAATGCGATTATT TTTT TTAATGATATA	-9.53
interaction.D ₃ 1_R0.6	TCAGTTCGGTGTACGCTTTCTAAAAGGCCGCGTTGCAAGGCCAAA TTTT AGTATAATCTAA	-10.15
interaction.D ₃ 2_R0.6	ACACGACTTATCGCTGTTCCGGGCGTTTCCCCCTGGGGTAATACG TTTT TTTAAAATTACT	-10.11
interaction.D ₄ 1_R0.6	TCTTCACCTAGATGGATTTTGCAGTATTTGGTATCTGGCCTAATC TTTT TTAGGATATTAT	-9.70
interaction.D ₄ 2_R0.6	AGCGATCTGTCTAAAGATCCTGCAGCAGATTACGCGTAACAGGAG TTTT GTATATCATTAA	-9.53
interaction.C ₁ _R0.6	CCATTCAGGCTGCAAGGGAAGGAACCATCACCCTAAGAGATAGGT TTTT ATTTGGATTGTG	-12.66
interaction.C ₂ _R0.6	CGTATTGGGCGCTAATGAGTGCTGGAGAATTCGCGCTCCCAGTCG TTTT AAGGGTTAGTAG	-12.52
interaction.C ₃ _R0.6	CAGCCCCACCGCTTGTCCGCCAAAAATCGACGCTCAGATAACGTG TTTT CATAGTTAACCC	-12.35
interaction.C ₄ _R0.6	TATGAGTAAACTTACGCTCAGAGCTCTTGATCCGGCGGCGGTGTT TTTT CACAATCCAAAT	-12.66
interaction.C ₅ _R0.6	ATCGTTGTCAGAATGGTGTCAAGAAGTGGTCCTGCAATACGGGTA TTTT CTACTAACCCCT	-12.52
interaction.C ₆ _R0.6	CTCATGAGCGGATGAGCAAAAAACGTTCTTCGGGGACCAAGTCG TTTT GGGTAACTATG	-12.35

Identifier	Sequence	ΔG (kcal/mol)
Interaction strands fiber $\epsilon_c/\epsilon_d = 0.5$		
interaction.D ₁ 1_R0.5	ACGCCAGCTGGCGGGGAAAGGAACCCCTAAAGGGAGAATCCCTCC TTTT TTCTATATAGAA	-10.98
interaction.D ₁ 2_R0.5	GCGTAACCACCACGGGCGCTGTGGACTCCAACGTCAGGAACAATT TTTT CCTATATATAGG	-10.99
interaction.D ₂ 1_R0.5	GCTGCGGCGAGCGGAAGCATATTATCCGCTCACAATGCGATTATT TTTT TAGTTAACTA	-10.92
interaction.D ₂ 2_R0.5	ACCTGTCGTGCCATGCGCTCAATTCGCGCTTGGCGTCCAGTGAGC TTTT GTTACGTAAC	-10.89
interaction.D ₃ 1_R0.5	ACACGACTTATCGCTGTTCCGGGCGTTCCTCCCTGGGGTAATACG TTTT AATCATGATT	-10.99
interaction.D ₃ 2_R0.5	TCAGTTCGGTGTACGCTTTCTAAAAGGCCGCGTTGCAAGGCCAAA TTTT ATCAATTGAT	-10.95
interaction.D ₄ 1_R0.5	AGCGATCTGTCTAAAGATCCTGCAGCAGATTACGCGTAACAGGAG TTTT AGATATATATCT	-10.94
interaction.D ₄ 2_R0.5	TCTTCACCTAGATGGATTTTGCAGTATTTGGTATCTGGCCTAATC TTTT AGTATATATACT	-10.84
interaction.C ₁ _R0.5	CCATTCAGGCTGCAAGGGAAGGAACCATCACCCCTAAGAGATAGGT TTTT AAAAAAATTAAG	-10.99
interaction.C ₂ _R0.5	CCATTCAGGCTGCAAGGGAAGGAACCATCACCCCTAAGAGATAGGT TTTT AAAAAATTTAAA	-10.88
interaction.C ₃ _R0.5	CCATTCAGGCTGCAAGGGAAGGAACCATCACCCCTAAGAGATAGGT TTTT AAAAATTTAAAAT	-10.83
interaction.C ₄ _R0.5	CCATTCAGGCTGCAAGGGAAGGAACCATCACCCCTAAGAGATAGGT TTTT CTTAATTTTTTTT	-10.99
interaction.C ₅ _R0.5	CCATTCAGGCTGCAAGGGAAGGAACCATCACCCCTAAGAGATAGGT TTTT TTTAAATTTTTTT	-10.88
interaction.C ₆ _R0.5	CCATTCAGGCTGCAAGGGAAGGAACCATCACCCCTAAGAGATAGGT TTTT ATTTTAATTTTTT	-10.83
AuNP linker strands		
AuNP_handle.1	GGGCGGCTGCTTGGTCTGCGAATTCTAAGCCTGGA AAAAAAAAAAAAAAAAAAAAA	
AuNP_handle.2	GCCCCTGCGTTCCGGAGGGCAAAAAGGCCAGGAACCG AAAAAAAAAAAAAAAAAAAAA	

Table S5: **Staple strand sequences for defect (D_{*Y*}X) and crystalline (C_{*Y*}) interactions used for modelling different energy ratios ϵ_c/ϵ_d .** Notations for interaction staples are the same as in Table S4 with an added R_{*Z*}. Here, *Z* represents the energy ratio ϵ_c/ϵ_d . Subsequences colored in dark and light blue represent defect and crystalline interaction strand extensions (see Fig. 3b of the main text). The rightmost column lists the Gibbs free energy change upon hybridization for each blue subsequence with its reverse complementary sequence.

-
- [1] M. E. Fornace, P. N. J., and N. A. Pierce, A unified dynamic programming framework for the analysis of interacting nucleic acid strands: Enhanced models, scalability, and speed, *ACS Synthetic Biology* **9**, 2665 (2020).
 - [2] J. N. Zadeh et al., Nupack: Analysis and design of nucleic acid systems, *Journal of Computational Chemistry* **32**, 170 (2011).
 - [3] D. Doty, B. L. Lee, and T. Stérin, scadnano: A browser-based, scriptable tool for designing DNA nanostructures, in *26th International Conference on DNA Computing and Molecular Programming (DNA 26)*, Leibniz International Proceedings in Informatics (LIPIcs), Vol. 174 (Schloss Dagstuhl – Leibniz-Zentrum für Informatik, 2020) pp. 9:1–9:17.
 - [4] J. Bohlin, M. Matthies, and E. Poppleton et al., Design and simulation of DNA, RNA and hybrid protein–nucleic acid nanostructures with oxview, *Nature Protocols* **17**, 1762 (2022).
 - [5] E. Poppleton, , M. Matthies, D. Mandal, F. Romano, P. Šulc, and L. Rovigatti, oxDNA: coarse-grained simulations of nucleic acids made simple, *Journal of Open Source Software* **8**, 4693 (2023).
 - [6] E. Poppleton, R. Romero, A. Mallya, L. Rovigatti, and P. Šulc, OxDNA.org: a public webserver for coarse-grained simulations of DNA and RNA nanostructures, *Nucleic Acids Research* **49**, W491 (2021).
 - [7] S. F. J. Wickham et al., Complex multicomponent patterns rendered on a 3d DNA-barrel pegboard, *Nature Communications* **11** (2020).
 - [8] B. Liu and J. Liu, Freezing directed construction of bio/nano interfaces: Reagentless conjugation, denser spherical nucleic acids, and better nanoflares, *Journal of the American Chemical Society* **139**, 9471 (2017).
 - [9] S. van der Walt, J. L. Schönberger, J. Nunez-Iglesias, F. Boulogne, J. D. Warner, N. Yager, E. Gouillart, T. Yu, and the scikit-image contributors, scikit-image: image processing in Python, *PeerJ* **2**, e453 (2014).
 - [10] N. D. Mermin, The topological theory of defects in ordered media, *Rev. Mod. Phys.* **51**, 591 (1979).